Brain-wide measurement of protein turnover with high spatial and temporal resolution

Boaz Mohar[1], Jonathan B. Grimm[1], Ronak Patel[1], Timothy A. Brown[1], Paul Tillberg[1], Luke D. Lavis[1], Nelson Spruston[1], Karel Svoboda[1,2]

1: HHMI Janelia Research Campus, Ashburn, VA; 2: Allen Institute for Neural Dynamics, Seattle, WA

Cellular functions are regulated by synthesizing and degrading proteins. This results in protein turnover on time scales ranging from minutes to weeks, varying across proteins, cellular compartments, cell types, and tissues. Current methods to track protein turnover lack the spatial and temporal resolution needed to investigate these processes, especially in the intact brain, which presents unique pharmacokinetic challenges. We describe a pulse-chase method (DELTA) to measure protein turnover with high spatial and temporal resolution throughout the body, including the brain. DELTA relies on the rapid covalent capture by HaloTag of fluorophores that were optimized for bioavailability *in vivo*. The nuclear protein MeCP2 showed brain region- and cell type-specific turnover. The synaptic protein PSD95 was shown to be destabilized in specific brain regions by behavioral enrichment. A novel variant of expansion microscopy enabled turnover measurements at individual synapses. DELTA will enable studies of adaptive and maladaptive plasticity in brain-wide neural circuits.

Introduction

Cellular functions are regulated by tuning transcription and translation to produce new proteins. Protein synthesis is balanced by protein degradation, which results in dynamic protein turnover[1]. In the brain, protein lifetimes range from tens of minutes for immediate early gene proteins[2] to months in the case of synaptic structural proteins[3]. Turnover rates vary by protein location or function, cell type, and brain region[4–6]. This dynamic process changes with environmental and behavioral conditions[6,7] and is modulated in neurodegenerative diseases[8]. Protein turnover is also necessary for animals to learn cognitive and motor tasks[9–11]. For example, learning is supported by long-term changes in synaptic strength that require both protein

synthesis[12,13] and degradation[14–16]. Protein turnover is regulated at multiple spatial scales in the brain. During learning and behavior, activity-dependent gene regulation is distributed throughout brain-wide neural circuits[17–19], but changes in synaptic strength are limited to active synapses[20–24], suggesting subcellular regulation of protein turnover. This combination of brain-wide and subcellular regulation calls for multiscale measurements of protein turnover *in vivo*.

Metabolic incorporation of modified amino acids followed by mass spectrometry allows the measurement of many proteins in parallel[25], but spatial resolution is limited to the level of brain regions (*e.g.*, cortex vs. cerebellum) or homogenate fractions (*e.g.*, cytoplasm vs. synaptosomes). Furthermore, results vary between individual studies depending on the cellular fraction selected and other experimental conditions (e.g. *in vitro* vs *in vivo*; for a review see Alvarez-Castelao & Schuman[26]). Alternatively, fluorescent imaging methods allow for labeling with different fluorophores at specific time points by fusing a tag with a protein of interest. This approach offers better spatial resolution, but remains difficult to deploy in the brain due to the need for epitope tags and labeled antibodies[27,28] or the self-labeling SNAP-tag[29] system and existing associated substrates, which do not cross the blood-brain barrier[30,31].

Here, we overcome these issues by using the HaloTag system (HT)[32] and cognate fluorescent ligands optimized for bioavailability, allowing the measurement of protein lifetime in the whole brain and other tissues *in vivo*. We first develop procedures for efficient labeling of HT with a panel of Janelia Fluor (JF) dyes attached to the HaloTag ligand (HTL)[33–35] in the mouse brain. Using spectrally separable dyes, we then developed a pulse-chase protocol to estimate protein lifetimes *in vivo*, which we named DELTA (**D**ye **E**stimation of the **L**ifetime of pro**T**eins in the br**A**in). We used simulations and calibration measurements to assess the theoretical sensitivity and precision of DELTA. We then used DELTA with the HaloTag protein fused to the nuclear transcriptional repressor protein MeCP2 and the synaptic scaffold protein PSD95 and measured the brain-wide protein turnover of these proteins at subcellular resolution. DELTA allows the measurement of protein turnover with unprecedented spatial and temporal resolution.

Results

Measuring protein turnover *in vivo* with high spatial and temporal resolution

We first modeled how a pulse-chase paradigm could be used to measure protein lifetime *in vivo* (**Fig. 1a**). We define two populations of HaloTag fusion proteins (protein-HT). *P* denotes the population labeled with the initial dye infusion (pulse), and *C* denotes the newly synthesized protein labeled with a later spectrally separable dye (chase). We assume that: (1) dye administrations are sufficient to saturate protein-HT, (2) dye clearance is much faster than protein turnover, and (3) protein degradation is exponential. Given these assumptions, we can calculate the mean lifetime of the protein: $\tau = \Delta T/\log(1/FP)$, where ΔT is the time interval between pulse and chase dye administration and *FP* is the fraction of the pulse-labeled part ($FP = P/[P + C]$). However, our assumptions may not be met in the context of real-life experiments, and the consequences on turnover measurements must be evaluated. For example, incomplete labeling of the protein during pulse dye injection, due to a more abundant target than the dye available to bind in the brain, would introduce a systematic underestimate of protein lifetime. Alternatively, dye excess and slow dye clearance (relative to the protein lifetime), would label newly synthesized proteins and thus produce an overestimate of the lifetime.

To quantify errors arising from invalidation of these assumptions, our model (**Extended Data Fig. 1**) included both dye kinetics (measured using *in vivo* imaging; **Supplementary Table 1**, **Extended Data Fig. 2**) and the injected dye-protein ratio as a measure of undersaturation or excess dye excess (dye/protein ratio of <1 or >1, respectively; **Fig. 1b**). We compared the measured lifetime and the simulated (true) lifetime using the following relation: $E=(\tau_{estimated} - \tau_{true})/\tau_{true} \times 100\%$. We found that undersaturation produces large errors, regardless of protein lifetime. In contrast, dye excess produces small errors, except for proteins with very short lifetimes (on the order of, or shorter than the extrusion time of ~82 min; **Extended Data Fig. 2**). These results show that the estimation errors are expected to be small if the labeling is saturated and the protein lifetime is longer than the mean dye clearance time. Furthermore, these biases would not change the relative measurements of protein lifetime between cell types, brain regions, or individual animals (see **Supplementary Note 1**).

To find dyes that efficiently bind protein-HT in mouse brains *in vivo* (**Methods**; **Extended Data Fig. 3; Supplementary Fig. 1**) we screened different JF-HTL compounds[33–35]. We expressed green fluorescent protein tagged with HT (GFP-HT) in mouse brains *in vivo*. JF-HTL dyes (**Supplementary Table 2**) were injected retro-orbitally, and after 12–18 hours we perfused the

brain with a spectrally orthogonal dye. With this approach, the unbound pulse dye has been cleared, protein degradation and synthesis are expected to be minimal, and the second dye will bind to any remaining unlabeled protein in the case of undersaturation. We used fraction pulse (FP) as a measure of the dye's ability to saturate the protein-HT target. Two dyes, JF_{669}-HTL and JF_{552}-HTL, were particularly bioavailable *in vivo* and displayed uniform labeling in the brain (**Supplementary Note 2; Supplementary Fig. 2**).

Measuring cell type and brain region – specific turnover of the nuclear protein MeCP2

Next, we measure the lifetime of methyl-CpG binding protein 2 (MeCP2), an abundant nuclear protein implicated in chromatin remodeling in neurons, and Rett syndrome[36–38]. We measured MeCP2 turnover by applying DELTA to MeCP2-HT knock-in mice[39]. Previous MeCP2 lifetime measurements using metabolic pulse-chase labeling provide a point of comparison for our method[6]. MeCP2 is a challenging case because it is expressed at high concentrations in all tissues. To assess saturation, JF_{669}-HTL was injected retro-orbitally (*P*), followed by perfusion of another dye ligand (C; JF_{585}-HTL) after one hour (**Extended Data Fig. 4a**). We imaged JF_{669}-HTL and JF_{585}-HTL fluorescence with subcellular resolution and at a brain-wide level. The lack of *C* staining indicated saturation with *P* dye in most harvested tissues, including most regions of the brain (**Extended Data Fig. 4b–h**). However, some brain regions with very dense cell body layers, were not saturated (*e.g.*, hippocampal CA1 region; **Extended Data Fig. 4i**). This is probably due to dye depletion and clearance of the dye before it could saturate these dense, MeCP2-HT-rich structures. Therefore, we excluded these brain regions from the analysis and focused on areas where MeCP2-HT was saturated by the pulse dye.

We sequentially injected highly bioavailable dyes (JF_{669}-HTL, JF_{552}-HTL), followed by perfusion of a third dye (JF_{608}-HTL) during tissue harvesting (**Fig. 1c**). This allowed us to compile multiple estimates of protein lifetime from the same animal (Methods). After perfusion, the brain was sectioned and stained with DAPI to identify all nuclei, and immunofluorescence (IF) was used to classify cell types (**Fig. 1c-d**). We imaged JF_{669}-HTL, JF_{608}-HTL, and JF_{552}-HTL fluorescence with subcellular resolution and calculated *FP* for all neuronal nuclei across the brain of five MeCP-HT mice. We segmented MeCP2 nuclei using Ilastik[40] and converted the measurements to average protein lifetime under the assumption of single exponential decay (**Methods**; **Fig. 1d**).

The lifetime of MeCP2 differed between brain regions. To assess the consistency of our method, we looked at pairwise correlations across animals for all commonly imaged brain regions (**Fig. 1e**, left and middle panel). The average mean correlation across pairs was high compared to shuffled controls for three levels of region annotation representing different spatial scales (5, 10, and 50 regions) based on the Allen Brain Reference common coordinate framework (CCFv3; **Extended Data Fig. 5a-c**)[41]. The largest outlier was the high stability of MeCP2 in the cerebellum (**Fig. 1e**, right panel), in agreement with a previous study[6]. Imaging consecutive coronal slices of the same cortical region, we also saw similar lifetimes of MeCP2-HT in neurons to those in oligodendrocytes and microglia when looking at consecutive coronal slices of the same brain region (**Extended Data Fig. 5d-f)** contrary to other reports[7]. These results demonstrate that the pulse-chase paradigm enables measurements of protein lifetime at subcellular resolution and brain-wide scales. The lifetime of MeCP2-HT varied between the brain regions but was consistent between animals under the same conditions and between different types of cells in the same cortical region.

PSD95 turnover is accelerated by behavioral enrichment

Next, we investigate the brain-wide dynamics of PSD95, a synaptic scaffold abundant in postsynaptic densities of excitatory synapses[42], using knock-in mice expressing PSD95 fused with HT (PSD95-HT)[43]. Because our goal is analysis down to the level of individual synapses, we developed an improved dye ligand: JFX_{673}-HTL (**Fig. 2a** and **Extended Data Fig. 6**). This dye is structurally similar to JF669-HTL, but contains deuterated pyrrolidine substituents instead of azetidines, an alteration that improves fluorophore brightness and photostability[35]. We discovered that this modification maintained the high bioavailability of its parent dye ligand, which is thought to be governed by chemical properties that are not affected by deuteration[34]. JFX_{673}-HTL saturated the HaloTag protein in the PSD95-HT knock-in mouse line (**Extended Data Fig. 6**).

Next, we measured the effects of behavioral manipulations on the half-life of PSD95-HT (**Fig. 2b**), using dye injection formulations optimized to saturate abundant PSD95-HT (**Supplementary Note 3** and **Methods**). Mice were separated into two groups: animals in the control group (n=2) were housed in isolation and animals in the second group (n=4) were housed in pairs in an enriched environment (EE)[44,45]. At the time of separation into groups, all mice received pulse dye (JFX_{673}-

144 HTL) and after two weeks, mice were perfused with a spectrally orthogonal chase dye (JF_{552}-
145 HTL). The brains were sectioned, imaged, registered to the Allen Brain Reference (CCFv3), and
146 the lifetime of PSD95 was calculated (**Fig. 2c**, **Methods**). PSD95-HT lifetime differed between
147 brain regions in both control and EE mice, as seen for example, between cortical layers and
148 hippocampal subfields (**Fig. 2d**; 1-way ANOVA, 6, F=105.91 p=6.7e-68). Looking more broadly,
149 we observed significant variability across different brain regions regardless of behavioral
150 enrichment (**Fig. 2e**; 1-way ANOVA, df=11, F=33.11, p=1.3e-51). Averaging across all brain
151 regions, the brain-wide average half-life of PSD95 was more than a day shorter (~10%) in mice
152 housed for two weeks in EE (**Fig. 2f**; average of all regions based on conditions: EE, magenta:
153 12.5±0.23 days n=4; control, green: 13.9±0.33 days n=2; ANOVA df=1, F=12.28 p=0.0248;
154 individual animals in light colors).

155 To determine whether EE produced nonuniform effects across brain regions, we compared
156 the differences between EE and control animals. We observed that the isocortex had the largest
157 difference (**Fig. 2g**, 1-way ANOVA, df=7, F=53.11, p=1.8e-55). We then examined different
158 cortical layers and subfields of the hippocampus. Although the lifetime followed a smooth gradient
159 with less stable PSD95-HT, the degree of destabilization was maximal in layer 4 (**Fig. 2h**; 1-way
160 ANOVA, df=6, F=3.4 p=0.003).

161 As we hypothesize that single synapses form the basis of learning in the brain[23], we
162 investigated PSD95-HT turnover in individual synapses. This requires an approximately four-fold
163 better resolution than that allowed by the classical diffraction limit. Expansion microscopy
164 (ExM)[46] allows for this four-fold enhancement, but uniform expansion requires dissolving the
165 native tissue structure through proteolysis or strong denaturation, leading to loss of signal (~50%
166 for antibodies or fluorescent proteins)[47]. Therefore, we developed an ExM protocol that would
167 enable twofold expansion without proteolysis or strong protein denaturation. We imaged the
168 expanded sample with Airyscan confocal microscopy[48], which provides another twofold
169 improvement in resolution, yielding an overall fourfold improvement in resolution (**Methods**).
170 Our use of bright and photostable small-molecule dyes, combined with the lack of any protein
171 disruption during expansion, enabled measurements of turnover at individual synapses. We applied
172 this method to different brain regions of one coronal section and were able to measure the turnover
173 in single synapses of cortical layer 1 and CA1, which had longer lifetimes than CA3 synapses (**Fig.**

2i; Supplementary Movie 3,4). This shows that DELTA has both brain-wide coverage and up to single-synapse resolution.

Discussion

DELTA enables the measurement of protein lifetime with unprecedented temporal and spatial precision throughout the body, including the brain, which presented special pharmacokinetic challenges. Using *in vivo* calibration measurements and *in situ* modeling, we defined the appropriate conditions for this pulse-chase paradigm in mice. We also introduced a new dye, JFX_{673}-HTL, with improved photophysical properties without compromising pharmacokinetics. Consistent with previous measurements using metabolic labeling, we found that MeCP2-HT protein turnover is slower in the cerebellum compared to other areas of the brain. We then measured the lifetime of the major excitatory synaptic scaffold protein PSD95 at a range of spatial scales from brain regions to single synapses. We found that PSD95-HT is destabilized by enriched experience, with cortical layers 2 to 5 as a major locus of plasticity.

DELTA is complementary to mass spectroscopy (MS)-based methods for measuring protein lifetime, with each method having distinct advantages and disadvantages. MS can measure 1000s of proteins in parallel but provides only low spatial resolution and works in homogenates. DELTA provides much higher spatial resolution but can only be used to analyze one protein at a time, limiting throughput and making simultaneous multiprotein measurements challenging. MS requires expensive equipment, while DELTA is cheaper. However DELTA requires genetically engineered animals and protein saturation tests (**Fig. 1b**) for each new knock-in mouse.

DELTA presents several advantages over previous methods and opportunities for extensions. The first is the spatial resolution range, from millimeters to ~100 nanometers—that can be achieved with a *post hoc* imaging-based approach. Second, the ability to combine turnover measurements with other imaging-based molecular methods such as fluorescence *in situ* hybridization (FISH)[49] or immunofluorescence (IF), which we have demonstrated for the identification of cell types. IF could also be used to identify other proteins to determine synaptic types or other subcellular compartments. Furthermore, DELTA could be combined with *in vivo* approaches such as the expression of indicators or actuators of neural activity to examine the relationship between neural activity and protein turnover.

DELTA could also be used to examine learning-related changes in synaptic proteins in the brain, including turnover measurements at the level of brain regions, cell types, specific input pathways, and individual synapses. This could also be done in both healthy mice and animal models of neurological disorders such as depression. Another application could involve measurements of activity *in vivo* with *ex vivo* protein lifetime measurements in the same cells to understand the effect of the history of activity on the changes in protein lifetime. Thus, this new method could help identify brain-wide changes involved in adaptive and maladaptive processes in an unbiased and high-throughput manner.

Methods

Materials

The purified HaloTag protein (#G4491) was purchased from Promega (Madison, Wisconsin). Pluronic F127 (# P3000MP), anhydrous DMSO (# D12345), TEMED (N,N,N′,N′-tetramethylethylenediamine; #15524010), APS (Ammonium Persulfate; #AAJ7632209), and AcX (Acryloyl-X SE; #A20770) were purchased from Thermo Fisher Scientific (Rockville, MD). Acrylamide (#1610140) and bis-acrylamide (#1610142) were purchased from Bio-rad (Hercules, CA). To obtain sodium acrylate, we neutralize acrylic acid purchased from TCI (Portland, OR; #A0141) with sodium hydroxide as previously described[50]. 4HT (4-Hydroxy-TEMPO; #176141-5G) was purchased from Sigma (Saint Louis, MO).

Animals

All procedures were carried out according to protocols approved by the Janelia Institutional Animal Care and Use Committee. Wild-type mice (C57Bl/6J RRID:IMSR_JAX:000664; both male and female) were housed in a 12:12 reverse light: dark cycle. MeCP2-HT[51] and PSD95-HT[43] knock-in mice of either sex were used. However, no comparisons were made between males and females for MeCP2-HT mice.

Virus, dye injections, and tissue processing

To evaluate the ability of JF dyes to saturate HT proteins in the brain, we needed sparse expression of an HT-labeled protein. We chose to express HaloTag-EGFP (HT-GFP) as many JF dyes are red or far red. Sparse brain expression and dye delivery were achieved using retroorbital

(RO) injections (Yardeni et al., 2011). Dye preparation[52], dye injections[53], and the histological preparations[54] are also described on protocols.io . HT-GFP virus was prepared using a PHP.eB AAV capsid (Chan et al. 2017) and a synapsin promoter. 100 µl of virus (titer of 4e11 GC/mL) was injected RO. An mKate-HaloTag was used to avoid cross- talk between the GFP and the JF_{525}-HTL dye. RO dye injections (pulse) were performed 3-5 weeks after virus injection. Most injections were prepared by dissolving 100 nmol of dye in 20 µl DMSO followed by 20 µl of 20% Pluronic F127 in DMSO and 60 µl of PBS, except when otherwise noted (Supplemental Table 2). Twenty-four hours after dye injection, animals were perfused with 50 ml of 4% PFA in 0.1 M sodium phosphate, pH 7.4 (PB) and 50 nmol of orthogonal dye. The brains were post-fixed in 4% PFA in 0.1 M PB overnight at 4 ° C and washed three times in PBS for 15 minutes. 100 µm coronal sections were cut and floated in 24-well plates followed by 4 h of DAPI staining (0.6 µM in PBS) and washed 3 times for 15 minutes in PBS. For animals with visible fluorescence from in vivo injection, every fourth slice was mounted for imaging; for animals where no fluorescence was observed, every 24th slice was mounted and imaged. See Supplementary Table 2 for details of the dyes and mounting of each of the animals in the study.

Expansion Microscopy

After sectioning, coronal sections were anchored with AcX (0.033 mg/ml; 1:300 from 10 mg/ml stock in DMSO) in PBS for one hour. Then they were moved to gelation solution containing: 2.7 M acrylamide, 0.2 M sodium acrylate, 200 µg/mL bis, PBS (1×), 2 mg/ml APS, 2 mg/ml TEMED, and 20 µg/mL 4HT. They were incubated on ice, shaking, for 30 minutes before being mounted in gelation chambers and moved to 37 ° C for one hour. After gelation, excess gel was trimmed, and the tissue was recovered in pure water. With three one-hour washes in pure water, the slices expanded ~2x without disruption or cracks. These sections were moved to a 6-well glass bottom plate (Cellvis #P06-1.5H-N, Mountain View, CA). To flatten and immobilize the sections, 4 dabs of silicon grease were applied around each section and a 22x22 mm square #2 coverslip (Corning #2855-22, Corning, NY) was pressed from above. If needed, poly-L-lysine 0.2 mg/ml (Sigma #P1524-25MG) with Photo-Flo 200 (1:500 from stock; #74257 Electron Microscopy Sciences, Hatfield, PA) were applied to the bottom of the well before the sections are placed to better immobilize the gels.

Whole-brain coronal section imaging

To image 6-20 coronal sections of tens of animals (i.e., hundreds of sections), we needed a high-throughput imaging platform. We used a confocal slide scanner consisting of a TissueFAXS 200 slide feeder (Tissuegnostics, Germany) and a SpectraX light engine (Lumencor) with the following peak powers and excitation filters: V – 395nm-400mW (395nm/25nm), C – 475nm-480mW (475nm/34nm), G/Y – lightpipe (585nm/35nm), R – 619nm-629mW (635nm/22nm). These were delivered by a lightguide to a Crest X-Light V2 confocal spinning disc microscope (Crestoptics; 60um pinhole spinning disk) with the following dichroics: T425lpxr, T495lpxt, T600lpxr, T660lpxr and emission filters: ET460nm/50nm, ET525nm/50nm, ET625nm/30nm, ET700nm/75nm. The emission light was collected with Zeiss objectives: EC Plan-Neofluar 2.5x/0.085 M27 for tissue detection, EC Plan-Neofluar 10x/0.3 M27 for MeCP2 and PSD95 animals (**Fig. 2c-h; Extended Data Fig. 4; Supplementary Fig. 5**) and a Plan-Apochromat 20x/0.8 M27 for virally injected animals (**Extended Data Fig. 3; Supplementary Fig. 1,2**). Detection was performed using a Zyla 5.5 sCMOS camera (Andor). The acquisition of the coronal sections was carried out after semi-automated tissue detection and by using multiple autofocusing points per section (5x5 and 3x3 grids for objective acquisitions of 20x and 10x accordingly). For virally transfected animals, three z-planes were imaged and z-projected with a 7 µm spacing. For MeCP2 and PSD95 animals, a single plane was imaged.

High-resolution imaging

To segment individual nuclei of MeCP2-HT-expressing cells (**Fig. 1d-f**; **Extended Data Fig. 5**) or single synapses expressing PSD95-HT (**Fig. 2i**), higher resolution imaging was needed. For MeCP2 imaging we used a Zeiss LSM 880 (Blackwood, NJ) with an EC Plan-Neoflour 40x/1.3NA oil objective and a voxel size of 0.25x0.25x0.5 µm. We acquired 21 z planes and 5 channels in 3 tracks. Detection [excitation] wavelengths were as follows (all in nm): Track 1 - DAPI: 410-489 [405]- DAPI, JF_{612}: 624-668 [594]; Track 2 IF: 493-551nm [488], JF_{669}: 680-758 [633]; Track 3 JF_{552}: 553-588 [561]. For PSD95 imaging we used a Zeiss LSM 980 with Airyscan and a C-Apochromat 40x/1.2 water dipping objective. The resulting pixel size after Airyscan processing was 57x57x230 nm. We acquired 23 z sections with two channels, 561 nm illumination for JF_{552}

and 633 nm illumination for JFX_{673}. A full z-stack was acquired for the far-red channel followed by the red channel.

Image analysis

JF Dye screening

We wanted to determine the amount of saturation for each dye injected *in vivo* (**Extended Data Fig. 3; Supplemental Figs. 1-3**). However, saturation must consider the amount of total protein (total = C+P), so the fraction pulse (FP) was used as a measure of saturation: FP = P/(C+P). Doing a pixel-wise analysis would not be sufficient, as there are background signals that would change depending on the imaged channel and brain region. Here, unlike knock-in animals, there is variability in the expression pattern across animals that could also affect the background (neruopil) in which the cells reside. Therefore, we chose to do a mask-based analysis for the cells along with a local background component that would avoid these confounding effects. To set masks, we imported 2x downsampled images with 3 channels (GFP-HT/P/C) into Ilastik's pixel classification workflow (Berg et al., 2019). The workflow was manually trained to segment cell bodies, dendrites, different types of neuropil signal, and different imaging and tissue artifacts. The pixel probabilities maps for cells, combined with the raw data, were then imported to a second object-classification workflow in Ilastik. This workflow was used to classify each mask as a GFP-HT-expressing cell or not. A Matlab script was used to calculate the value of each mask in the three channels and also to calculate a local background. The local background estimation excluded pixels that belonged to other non-neuropil trained categories (other cells, dendrites, etc.) from the first Ilastik workflow (**Extended Data Fig. 3c; Supplemental Fig. 1**). For each mask, a background subtracted value was calculated for each dye and converted to µM dye concentration using an independent calibration obtained under the same imaging conditions (**Supplemental Fig. 3**). FP was calculated after conversion to µM dye, where FP values closer to 1 indicate saturation.

MeCP2

To segment MeCP2-HT nuclei and categorize them into cell types using immunofluorescence (IF), a modified Ilastik classification pipeline was used (**Fig. 1c,d; Extended Data Fig. 5**). First, the five imaged channels (DAPI, Pulse, Chase1, Chase2, IF) were each normalized from 0 to 1 using the top and bottom 0.3% of the histogram. Second, a mean of all three imaged JF dyes was

used to make a 3-channel image (DAPI, mean of all JF dyes, IF). This was used in the Ilastik pixel classification workflow. We used training data from all three types of IF used (NeuN, Iba1 and SOX10). The resulting nuclei probability maps in combination with the 3-channel images were used by three independent object classification workflows in Ilastik, one for each IF type. The output of these three workflows was a set of masks indicating IF-positive nuclei for each cell type. These were used as described above to extract FP. Next, a mean lifetime (τ) was calculated with the assumption of a single exponential decay given our pulse-chase interval (ΔT): $\tau = \Delta T / \log(\frac{1}{FP})$.

Brain-wide PSD95 analysis

To assign PSD95 lifetimes across the brain, we performed a pixel-based analysis (**Fig. 1b-h**), as there is no way to segment individual objects (synapses) from our low-resolution imaging. As with MeCP2, we converted our images to 3-channel images (DAPI/P/C) after 2x downsampling and normalization to saturate the 0.3% top and bottom of each channel's histogram. These were then imported to an ilastik pixel-classification workflow that was trained to detect places where synapses are a meaningful signal (i.e., excluding non-tissue, artifacts, ventricles). The result was used as a mask on the original data. As in MeCP2 analysis, each pixel was converted to a lifetime estimate with the assumption of a single exponential decay after conversion to µM dye concentration using calibration curves imaged under the same conditions.

Expansion microscopy

After acquisition using the Airyscan detector array, we used Zen Blue software (Zeiss) to process the images using a 3d reconstruction of each channel with automated deconvolution strength. The Airyscan-processed images were registered across channels as they were acquired sequentially. Shifts between channels were under 3 pixels. The resulting 2-channel image was normalized and used as input to an Ilastik pixel classification pipeline trained to separate synapses from the background. The resulting probability images with the normalized data were used in a second Ilastik object segmentation pipeline. Here synapses were classified as simple (single line) or complex (rings, multiple curves). Both classes were used (**Fig. 2i**). As we had segmented objects, we could subtract a local background, use a calibration to convert the values to µM dye, and get an estimated lifetime assuming a single exponential decay.

Alignment to the Allen CCF

To align both MeCP2 and PSD95 lifetime measurements with the Allen CCF, a two-step procedure was used. First, a 24-bit downsampled (max 1.5Mb with png) 24-bit RGB image of each section was generated. It was loaded with QuickNII[55] and aligned with version 3 of Allen CCF at a resolution of 25 μm resolution. This was able to account for the cutting angle, a global scaling factor in the DV and ML axis, and the AP location of each section. QuickNII output was used for a manual non-rigid alignment with VisuAlign[56]. The main markers for alignment were the edges of the section, the ventricles, and the fiber tracks. The VisuAlign output was another RGB image in which each color was assigned to an Allen Institute CCF id. These images were loaded and interpolated to the original size of each section, allowing the assignment of each MeCP2 nucleus and PSD95 pixel to a CCF id. As the PSD95 analysis was pixel based, we excluded any pixel belonging to the root or any part of the CCF tree under fiber tracks or ventricular system.

Dye clearance

Cranial windows were made on ALM or V1 (centered on - 2.5 mm lateral, + 0.5 mm anterior from lambda) and a headbar was attached posterior to the window as previously described[57]. The animals were anesthetized in 1% isoflurane and kept at 37 °C with a heating pad. The optical setup was the same as previously described[58], with a custom wide-field fluorescence microscope (Thorlabs) and a sCMOS camera (Hamamatsu Orca Flash 4.0 v3). Details of illumination, objectives, and filters are presented in Supplementary Table 1. A baseline image was acquired before dye injection. Both the baseline and subsequent timepoints were acquired as movies of 40-50 frames at 5 Hz. This was done to reduce the chances of saturating pixels on the camera at the peak on the injection while still being above electrical noise under baseline conditions. The animal was then removed from head fixation and injected with dye. After dye injection, it was quickly returned to head fixation; the field of view was compared to a baseline image under room lights and then imaged for up to four hours in intervals of 2 minutes to 20 minutes to cover the fast decay part of the dye clearance. The animal was then recovered and reimaged for up to 24 h at 4-12 h intervals.

The images were analyzed using a custom Matlab script (Github). Briefly, each movie was averaged and a manual ROI was defined (**Extended Data Fig. 2b**). The pixel-averaged mean was

fitted to a double exponential: $F = \boldsymbol{a} * \boldsymbol{e}^{-\mathbf{1}/\boldsymbol{\tau_1}} + \boldsymbol{b} * \boldsymbol{e}^{-\mathbf{1}/\boldsymbol{\tau_2}} + \boldsymbol{c}$. Population averages were computed by binning all 11 experiments together. In cases where the injection phase was captured, an offset was used to start the fitting from the highest time point.

Carotid artery dye infusion

To measure the infusion kinetics of JF dyes, we needed a way to control the rate of infusion while imaging dye accumulation in the brain through a cranial window (**Supplemental Fig. 4**). We used two C57Bl/6j animals with common carotid artery vascular catheterization. These were ordered from Charles Rivers as a surgical service. They were flushed with saline and 50% sucrose lock solution every 7 days. A cranial window was performed 7 days after catheterization as described above. 7 days after cranial window surgery, a JF dye pump was connected to the carotid artery line. The initial pump rate was 20 ul/min followed by 40 ul/min and 80 ul/min. The imaging conditions were the same as for the dye clearance experiments (0.2 s exposure) but imaged continuously for each injection speed. Data were time averaged at 1 s (5 timepoints) and a manual ROI was drawn. The time-averaged fluorescence values were trimmed to the times the pump was running and fit with a linear fit (including intercept). The values reported are the slopes of the fit.

Modeling dye clearance effects on saturation

Given our results on dye infusion (**Supplementary Note 3; Supplementary Fig.4**), we wanted to test the hypothesis that given a fixed amount of dye to inject, faster injections would lead to more dye captured in the brain. We considered a simple model where a single position in space (x position 1) is a blood vessel from which dye can enter the system and diffuse in 1D simulated by a time march (using Fourier's equation). To avoid edge conditions (Dirichlet boundary conditions were simulated) care was taken to simulate all relevant dye diffusion away from the edge. Both dye injection and clearance were simulated at the same arbitrary rate (dt). All simulations had the same total amount of dye injected, and a constant amount of dye was cleared from the vessel at a rate of 1AU/dt. Different simulations had different injection rates (2-10 AU/dt) and the width of the dye distribution was measured as the width in dx at 90% of the known saturation value. Code is available online (GitHub).

Modeling protein turnover measurements with DELTA

Pulse-chase experiments were modeled using the SimBiology package in Matlab (Mathworks; GitHub link). Briefly, lifetimes of the target HT-protein synthesis were simulated. Each new protein could either degrade (at the same rate of synthesis modeled) or attach to a HaloTag ligand dye molecule (Pulse or Chase, dye collectively). The dye binding kinetics were set to be nearly instantaneous, as they are several orders of magnitude higher than those for synthesis/degradation. Binding kinetics were identical for both the Pulse and Chase. The degradation rates of the HT protein with dye complexes were the same as for the protein alone.

The dye injection kinetics were neglected (i.e., instantaneous injection). Dye clearance kinetics were modeled as two compartments (named Brain & Lipids) with degradation from the Brain compartment. This was done to account for the multiexponential decay measured *in vivo*. The Brain compartment was set to have a volume of 1 ml; the equilibrium constant between the compartments, the volume of the Lipids compartment and the degradation time constant were fitted using the JF-dyes clearance data (**Extended Data Fig. 1,2**). This fitting was done in the absence of a HT-protein.

Dye solubility

Formulations for the solubility measurements of the JF dyes were prepared in the following manner. (i) 30% Captisol formulation was made with 300 mg Captisol® (β-Cyclodextrin Sulfobutyl Ethers, sodium salts) (NC-04A-180186, Cydex Pharmaceuticals) dissolved in 1 ml of sterile water (Molecular Biology Grade Water, Corning) to make a 30% solution. 100 µl of this solution was added to 100 nmol of dry JF dye. (ii) A 30% Captisol + Pluronic formulation was made by mixing a 30% Captisol solution with Pluronic F-127 (P3000MP, Invitrogen) in a 80:20 ratio. 100 µl of the prepared solution was added to 100 nmol of dry JF dye. (iii) The DMSO + Pluronic formulation was made with DMSO (D2650, Sigma Aldrich), Pluronic F-127, and sterile saline (0.9 % sodium chloride) mixed in a 20:20:60 ratio. 100 µl from the prepared solution was added to 100 nmol of dry JF dye. (iv) A formulation of DMSO only was made by adding 100 µl of DMSO to 100 nmol of dry JF dye to bring it to a final concentration of 1 mM.

The prepared JF dye formulations were briefly vortexed followed by bath sonication (Branson 1200 model) for 5 minutes. The dye solutions were placed on the agitator for 72 h to ensure solubilization. Absorbance measurements of dye solutions were performed using a spectrometer

(Cary 100 UV-Vis, Agilent Technologies), and the final concentration was determined from known extinction coefficients of JF dyes as defined by Grimm et al. [33–35].

Data and Code availability

Both metadata and raw data are available through the Open Science Foundation project associated with this paper. The protocols are available as a collection on protocols.io. The code used for the analysis is available on GitHub.

References

1. Alberts, B. *et al. Essential cell biology*. (W. W. Norton & Company, 2019).
2. Soulé, J. *et al.* Balancing Arc synthesis, mRNA decay, and proteasomal degradation: maximal protein expression triggered by rapid eye movement sleep-like bursts of muscarinic cholinergic receptor stimulation. *J. Biol. Chem.* **287**, 22354–22366 (2012).
3. Heo, S. *et al.* Identification of long-lived synaptic proteins by proteomic analysis of synaptosome protein turnover. *Proc. Natl. Acad. Sci.* **115**, E3827–E3836 (2018).
4. Alvarez-Castelao, B., Schanzenbächer, C. T., Langer, J. D. & Schuman, E. M. Cell-type-specific metabolic labeling, detection and identification of nascent proteomes in vivo. *Nat. Protoc.* **14**, 556–575 (2019).
5. Cohen, L. D. & Ziv, N. E. Neuronal and synaptic protein lifetimes. *Curr. Opin. Neurobiol.* **57**, 9–16 (2019).
6. Fornasiero, E. F. *et al.* Precisely measured protein lifetimes in the mouse brain reveal differences across tissues and subcellular fractions. *Nat. Commun.* **9**, 1–17 (2018).
7. Dörrbaum, A. R., Kochen, L., Langer, J. D. & Schuman, E. M. Local and global influences on protein turnover in neurons and glia. *eLife* **7**, e34202 (2018).
8. Paterson, R. W. *et al.* SILK studies — capturing the turnover of proteins linked to neurodegenerative diseases. *Nat. Rev. Neurol.* **15**, 419–427 (2019).

9. Flexner, J. B., Flexner, L. B. & Stellar, E. Memory in Mice as Affected by Intracerebral Puromycin. *Science* **141**, 57–59 (1963).

10. Luft, A. R., Buitrago, M. M., Ringer, T., Dichgans, J. & Schulz, J. B. Motor Skill Learning Depends on Protein Synthesis in Motor Cortex after Training. *J. Neurosci.* **24**, 6515–6520 (2004).

11. Park, H. & Kaang, B.-K. Balanced actions of protein synthesis and degradation in memory formation. *Learn. Mem.* **26**, 299–306 (2019).

12. Kelleher, R. J., Govindarajan, A., Jung, H.-Y., Kang, H. & Tonegawa, S. Translational Control by MAPK Signaling in Long-Term Synaptic Plasticity and Memory. *Cell* **116**, 467–479 (2004).

13. McGaugh, J. L. Memory--a Century of Consolidation. *Science* **287**, 248–251 (2000).

14. Fioravante, D. & Byrne, J. H. Protein degradation and memory formation. *Brain Res. Bull.* **85**, 14–20 (2011).

15. Fonseca, R., Vabulas, R. M., Hartl, F. U., Bonhoeffer, T. & Nägerl, U. V. A Balance of Protein Synthesis and Proteasome-Dependent Degradation Determines the Maintenance of LTP. *Neuron* **52**, 239–245 (2006).

16. Lee, S.-H. *et al.* Synaptic Protein Degradation Underlies Destabilization of Retrieved Fear Memory. *Science* **319**, 1253–1256 (2008).

17. DeNardo, L. A. *et al.* Temporal evolution of cortical ensembles promoting remote memory retrieval. *Nat. Neurosci.* **22**, 460–469 (2019).

18. Roy, D. S. *et al.* Brain-wide mapping reveals that engrams for a single memory are distributed across multiple brain regions. *Nat. Commun.* **13**, 1799 (2022).

19. Ye, L. *et al.* Wiring and Molecular Features of Prefrontal Ensembles Representing Distinct Experiences. *Cell* **165**, 1776–1788 (2016).

20. Bliss, T. V. & Lomo, T. Long-lasting potentiation of synaptic transmission in the dentate area of the anaesthetized rabbit following stimulation of the perforant path. *J. Physiol.* **232**, 331–356 (1973).

21. Frey, U. & Morris, R. G. M. Synaptic tagging and long-term potentiation. *Nature* **385**, 533–536 (1997).

22. Harvey, C. D. & Svoboda, K. Locally dynamic synaptic learning rules in pyramidal neuron dendrites. *Nature* **450**, 1195–1200 (2007).

23. Matsuzaki, M., Honkura, N., Ellis-Davies, G. C. R. & Kasai, H. Structural basis of long-term potentiation in single dendritic spines. *Nature* **429**, 761–766 (2004).

24. Nabavi, S. *et al.* Engineering a memory with LTD and LTP. *Nature* **511**, 348–352 (2014).

25. Chen, X., Wei, S., Ji, Y., Guo, X. & Yang, F. Quantitative proteomics using SILAC: Principles, applications, and developments. *PROTEOMICS* **15**, 3175–3192 (2015).

26. Alvarez-Castelao, B. & Schuman, E. M. The Regulation of Synaptic Protein Turnover. *J. Biol. Chem.* **290**, 28623–28630 (2015).

27. Butko, M. T. *et al.* Fluorescent and photo-oxidizing TimeSTAMP tags track protein fates in light and electron microscopy. *Nat. Neurosci.* **15**, 1742–1751 (2012).

28. Lin, M. Z., Glenn, J. S. & Tsien, R. Y. A drug-controllable tag for visualizing newly synthesized proteins in cells and whole animals. *Proc. Natl. Acad. Sci.* **105**, 7744–7749 (2008).

29. Keppler, A. *et al.* A general method for the covalent labeling of fusion proteins with small molecules in vivo. *Nat. Biotechnol.* **21**, 86–89 (2003).

30. Bojkowska, K. *et al.* Measuring In Vivo Protein Half-Life. *Chem. Biol.* **18**, 805–815 (2011).

31. Hawkins, B. T. & Egleton, R. D. Fluorescence imaging of blood-brain barrier disruption. *J. Neurosci. Methods* **151**, 262–267 (2006).

32. Los, G. V. *et al.* HaloTag: a novel protein labeling technology for cell imaging and protein analysis. *ACS Chem. Biol.* **3**, 373–382 (2008).

33. Grimm, J. B. *et al.* A general method to fine-tune fluorophores for live-cell and in vivo imaging. *Nat. Methods* **14**, 987–994 (2017).

34. Grimm, J. B. *et al.* A general method to optimize and functionalize red-shifted rhodamine dyes. *Nat. Methods* **17**, 815–821 (2020).

35. Grimm, J. B. *et al.* A General Method to Improve Fluorophores Using Deuterated Auxochromes. *JACS Au* **1**, 690–696 (2021).

36. Ehrhart, F. *et al.* Rett syndrome – biological pathways leading from MECP2 to disorder phenotypes. *Orphanet J. Rare Dis.* **11**, (2016).

37. Qiu, Z. *et al.* The Rett Syndrome Protein MeCP2 Regulates Synaptic Scaling. *J. Neurosci.* **32**, 989–994 (2012).

38. Zimmermann, C. A., Hoffmann, A., Raabe, F. & Spengler, D. Role of Mecp2 in Experience-Dependent Epigenetic Programming. *Genes* **6**, 60–86 (2015).

39. Piccolo, F. M. *et al.* Mecp2 Nuclear Dynamics in Live Neurons Results from Low and High Affinity Chromatin Interactions. *SSRN Electron. J.* (2019) doi:10.2139/ssrn.3376659.

40. Berg, S. *et al.* ilastik: interactive machine learning for (bio)image analysis. *Nat. Methods* **16**, 1226–1232 (2019).

41. Wang, Q. *et al.* The Allen Mouse Brain Common Coordinate Framework: A 3D Reference Atlas. *Cell* **181**, 936-953.e20 (2020).

42. Cho, K.-O., Hunt, C. A. & Kennedy, M. B. The rat brain postsynaptic density fraction contains a homolog of the drosophila discs-large tumor suppressor protein. *Neuron* **9**, 929–942 (1992).

43. Masch, J.-M. *et al.* Robust nanoscopy of a synaptic protein in living mice by organic-fluorophore labeling. *Proc. Natl. Acad. Sci.* **115**, E8047–E8056 (2018).

44. Nithianantharajah, J. & Hannan, A. J. Enriched environments, experience-dependent plasticity and disorders of the nervous system. *Nat. Rev. Neurosci.* **7**, 697–709 (2006).

45. Rosenzweig, M. R. & Bennett, E. L. Effects of differential environments on brain weights and enzyme activities in gerbils, rats, and mice. *Dev. Psychobiol.* **2**, 87–95 (1969).

46. Chen, F., Tillberg, P. W. & Boyden, E. S. Expansion microscopy. *Science* **347**, 543–548 (2015).

47. Tillberg, P. W. *et al.* Protein-retention expansion microscopy of cells and tissues labeled using standard fluorescent proteins and antibodies. *Nat. Biotechnol.* **34**, 987–992 (2016).

48. Huff, J. The Airyscan detector from ZEISS: confocal imaging with improved signal-to-noise ratio and super-resolution. *Nat. Methods* **12**, i–ii (2015).

49. Wang, Y. *et al.* EASI-FISH for thick tissue defines lateral hypothalamus spatio-molecular organization. *Cell* **184**, 6361-6377.e24 (2021).

50. Damstra, H. G. *et al.* Visualizing cellular and tissue ultrastructure using Ten-fold Robust Expansion Microscopy (TREx). *eLife* **11**, e73775 (2022).

51. Piccolo, F. M. *et al.* Mecp2 Nuclear Dynamics in Live Neurons Results from Low and High Affinity Chromatin Interactions. *SSRN Electron. J.* (2019) doi:10.2139/ssrn.3376659.

52. Mohar, B. Preparation of JF dye for retro-orbital injection in mice. *protocols.io* https://www.protocols.io/view/preparation-of-jf-dye-for-retro-orbital-injection-5u4g6yw (2019).

53. Mohar, B. *Retro-orbital injection of virus or dye in mice v1*. https://www.protocols.io/view/retro-orbital-injection-of-virus-or-dye-in-mice-5udg6s6 (2019) doi:10.17504/protocols.io.5udg6s6.

54. Mohar, B. & Copeland, M. *Protocol for mouse perfusion with dye, DAPI staining, and slide preparation v1*. https://www.protocols.io/view/protocol-for-mouse-perfusion-with-dye-dapi-stainin-59jg94n (2019) doi:10.17504/protocols.io.59jg94n.

55. QuickNII; RRID:SCR_016854; http://www.nitrc.org/projects/quicknii/. (2022).

56. VisuAlign; RRID:SCR_017978; http://www.nitrc.org/projects/visualign/. (2021).

57. Ashby, M. C. *et al.* Removal of AMPA Receptors (AMPARs) from Synapses Is Preceded by Transient Endocytosis of Extrasynaptic AMPARs. *J. Neurosci.* **24**, 5172–5176 (2004).

58. Abdelfattah, A. S. *et al.* Bright and photostable chemigenetic indicators for extended in vivo voltage imaging. *Science* **365**, 699–704 (2019).

59. Yardeni, T., Eckhaus, M., Morris, H. D., Huizing, M. & Hoogstraten-Miller, S. Retro-orbital injections in mice. *Lab Anim.* **40**, 155–160 (2011).

60. Holtmaat, A. *et al.* Long-term, high-resolution imaging in the mouse neocortex through a chronic cranial window. *Nat. Protoc.* **4**, 1128–1144 (2009).

61. Trachtenberg, J. T. *et al.* Long-term in vivo imaging of experience-dependent synaptic plasticity in adult cortex. *Nature* **420**, 788–794 (2002).

62. Walther, D. M. & Mann, M. Accurate Quantification of More Than 4000 Mouse Tissue Proteins Reveals Minimal Proteome Changes During Aging *. *Mol. Cell. Proteomics* **10**, S1–S7 (2011).

63. Zhao, Y., Denner, L., Haidacher, S. J., LeJeune, W. S. & Tilton, R. G. Comprehensive analysis of the mouse renal cortex using two-dimensional HPLC – tandem mass spectrometry. *Proteome Sci.* **6**, 15 (2008).

64. Chan, K. Y. *et al.* Engineered AAVs for efficient noninvasive gene delivery to the central and peripheral nervous systems. *Nat. Neurosci.* **20**, 1172–1179 (2017).

65. Verkhusha, V. V. *et al.* High Stability of Discosoma DsRed As Compared to Aequorea EGFP. *Biochemistry* **42**, 7879–7884 (2003).

66. Caujolle, F., Caujolle, D., Bouyssou, H. & Calvet, M. M. Toxicity and pharmacological aptitudes of Dimethylsulfoxide. *Comptes Rendus Hebd. Seances Acad. Sci.* **258**, 2224–2226 (1964).

67. Krenzlin, H., Lorenz, V., Danckwardt, S., Kempski, O. & Alessandri, B. The Importance of Thrombin in Cerebral Injury and Disease. *Int. J. Mol. Sci.* **17**, 84 (2016).

Acknowledgments

Histology: Benjamin Foster, Monique Copeland, Amy Hu, Susan Michael; Imaging core: Michael DeSantis, Damien Alcor; Vivarium: Gillian Harris, Mariam Rose, Sarah Lindo; Viral core: PHP virus; T3 (bleaching): Ariana Tkachuk; Open chemistry: Anastasia Osowski, Katie Holland; GFP-HT virus: Eric Schreiter; MeCP2-HT animal: James Liu; PSD95-HT animal: Seth Grant; Clearance imaging: Amrita Singh

Figures

Figure 1 – Measurement of protein turnover *in vivo*, demonstrated with MeCP2

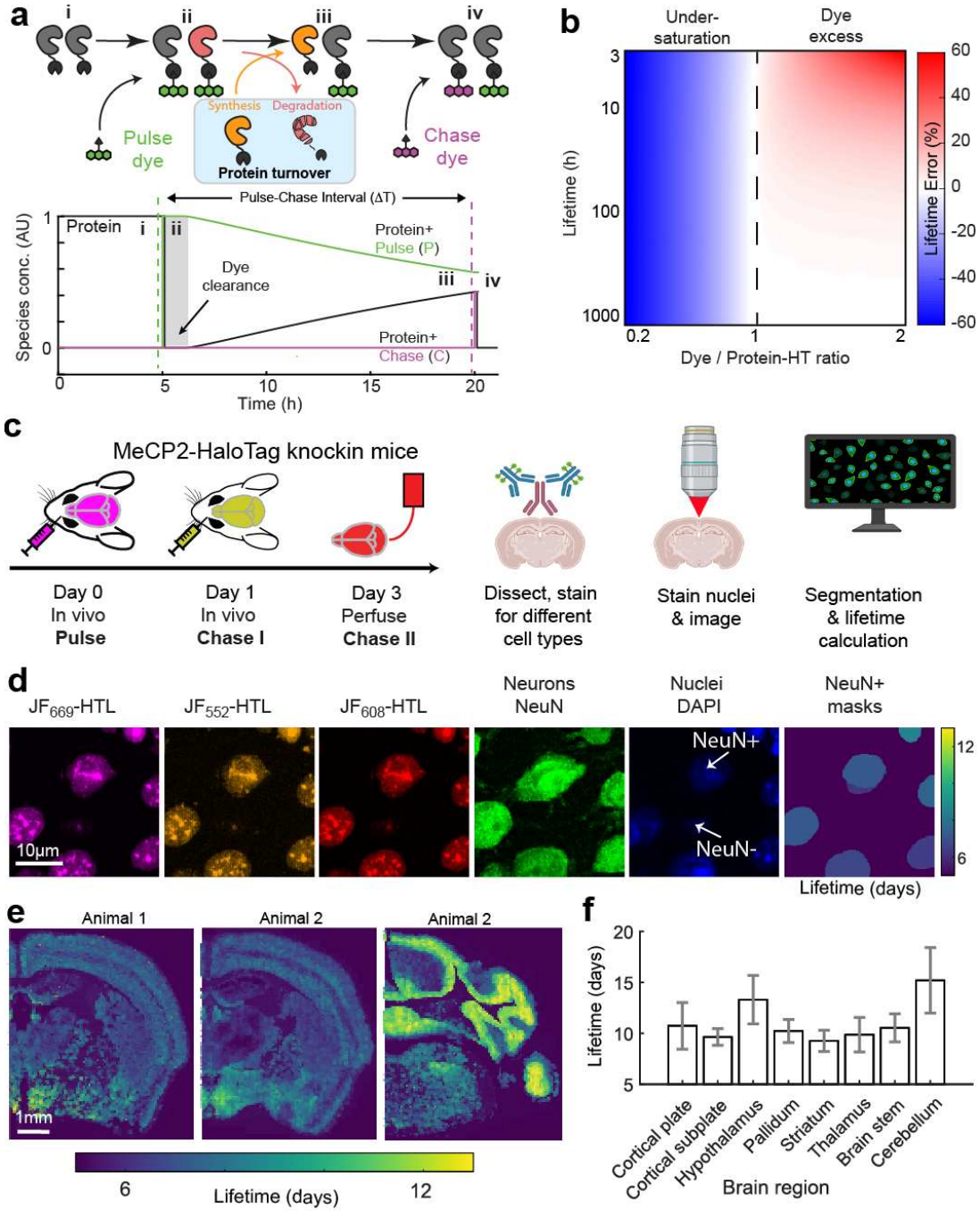

a, Schematics showing dye capture by a protein modified with a HaloTag (HT). (i) Before the injection of the first dye ligand (pulse), there is no label on the protein (black line). (ii) After injection of the first dye (dashed green line at 5 h), all proteins are labeled with the pulse (solid green line). (iii) During the pulse-chase interval, some proteins degrade, and others are synthesized (termed protein turnover) but are unlabeled. (iv) Injection of a spectrally separate dye (dashed magenta line at 20 h) captures the newly synthesized fraction (solid magenta line). The arrow and gray shaded area indicate where excess dye delays the onset of turnover measurement, leading to an overestimation error. **b**, Simulation with different dye-protein ratios (x-axis) and true lifetimes (y-axis). The estimated lifetime is colored. Undersaturation (left side <1 dye/protein ratio) causes worse errors than dye excess (right side >1 dye/protein ratio) and longer-lived proteins (>10 h) are better estimated than short-lived ones. **c,** Schematic of the procedure to measure the turnover of the nuclear MeCP2-HT protein in a knock-in mouse model. Three dyes were used to measure multiple protein-turnover intervals. After perfusion and dissection, coronal sections were stained with IF to identify different cell types, while DAPI was used as a nuclear marker. **d,** Example field of view showing all JF dyes (left 3 panels) imaged with an example NeuN stained coronal section (4^{th} panel) to identify neurons alongside all nuclei (DAPI; 5^{th} panel). After segmentation of NeuN positive nuclei (6^{th} panel), segmented nuclei were colored by lifetime using the sum of the two *in vivo* injections as the pulse (JF_{669}+JF_{552} / JF_{669}+JF_{552}+JF_{608}). **e,** Example coronal sections from 2 animals showing the consistency of the lifetime estimate for the same AP section (compare left and middle panel) and differences across brain regions, most notably the longer lifetime in the cerebellum (compare middle and right panels). **f,** lifetime means, and bootstrap confidence intervals for CCF-aligned brain regions of MeCP2.

Figure 2 – PSD95 turnover depends on experience

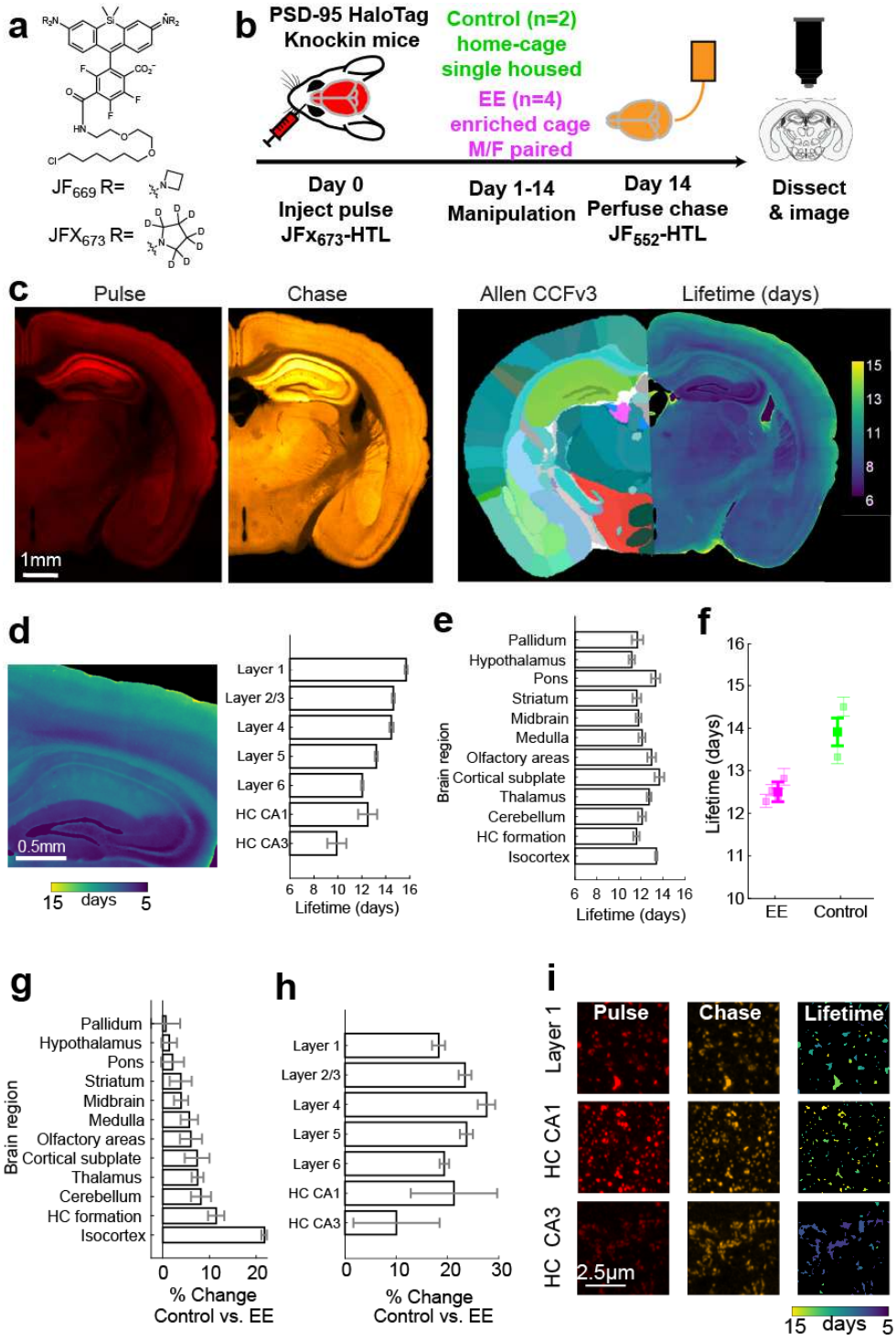

a, Structure of JF_{669}-HTL and the new JFX_{673}-HTL. Note the replacement of deuterium and additional carbon in the R position. **b,** Schematic of the procedure to measure the turnover of

synaptic PSD95-HT protein in a knock-in mouse. After initial injection of the new JFX_{673} animals were separated to be single housed (n=2) or male/female paired in an enriched environment (EE, n=4) for 14 days. At the end of 2 weeks, the animals were perfused with JF_{552}, sectioned, imaged, and aligned with the Allen Institute CCFv3 mouse brain atlas. **c,** Example coronal section showing the pulse (left panel), chase (middle panel), and calculated lifetime aligned to the Allen CCFv3 (right panel). **d,** Left: zoom-in of the image from panel c. Note the lifetime gradient that separates the CA1 *stratum radiatum* (long lifetime) and CA1 *stratum lacunosum moleculare*, dentate gyrus *stratum moleculare,* and hilus (all short lifetime). Right: Average lifetime of different cortical layers and subfields of the hippocampus (HC). **e**, Average lifetime for 12 large brain regions. **f,** Average lifetime of the 4 animals under EE (magenta) and control conditions (green). EE increased protein turnover and shortened the average lifetime of PSD95. Individual animals in lighter colors. **g,** Percent change in control vs. EE animals in the cortical layers. **h,** same as **g** for 12 different brain regions. **i,** Example images using Airyscan imaging of ExM tissue (max projection of 5 z planes 0.3 um apart) from layer 1 (top row), HC CA1 subfield (middle row) and basal dendrites of CA3 (bottom row) showing both pulse (left columns), chase (middle columns) and lifetime (left columns).

Extended Data Figures

Extended Data Figure 1 – Modeling pulse-chase experiments *in vivo* constrained by dye clearance measurements

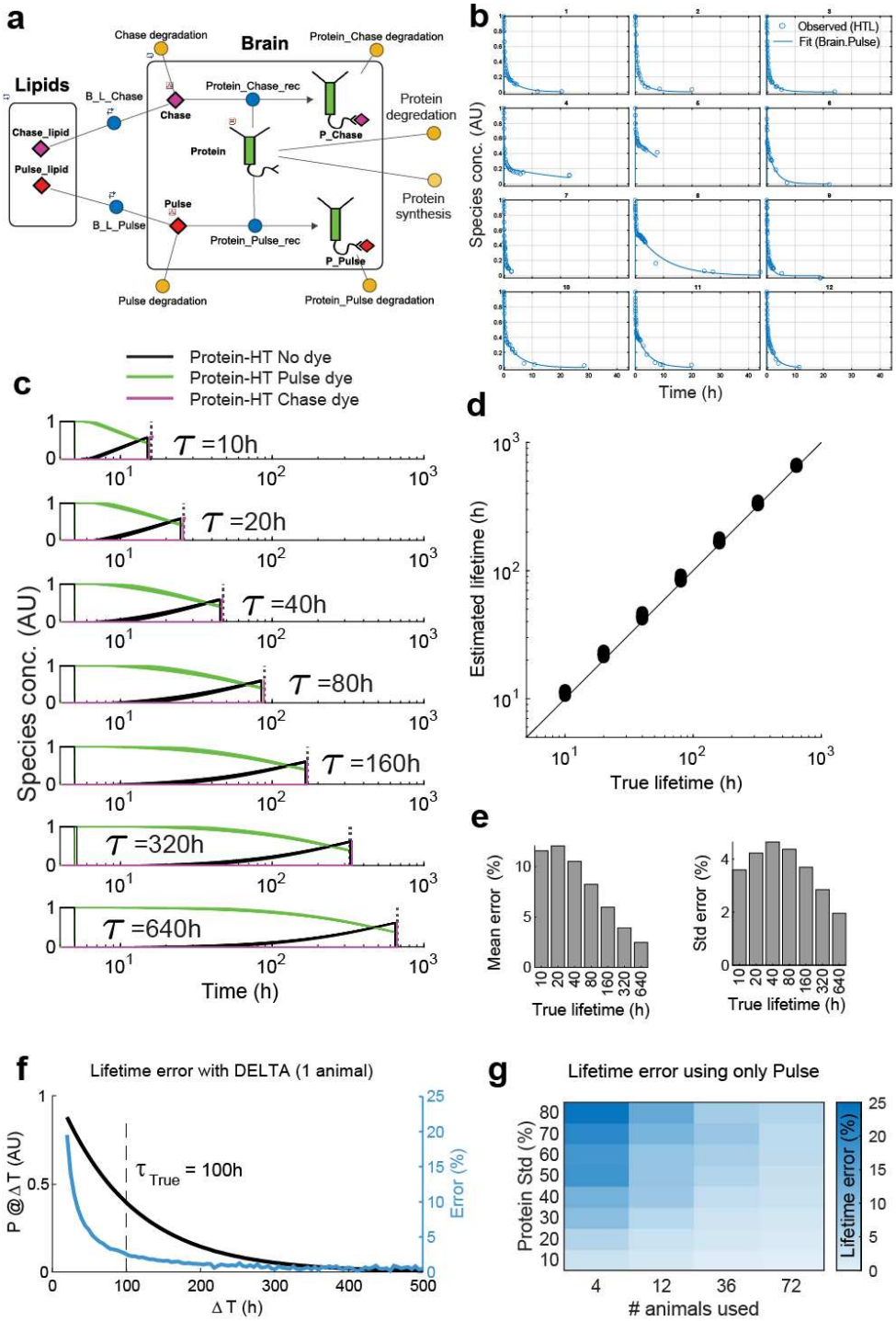

626 **a**, Schematic showing model compartments, reactions, and species for investigating the effects
627 of dye clearance in protein turnover measurements. **b**, Fitting of the *in vivo* dye clearance data to
628 generate model variants. 12 experiments (data in blue circles) and the fitted response (black line)
629 are shown. **c-e,** Example model simulations with 7 lifetimes (**c**: 10-640h) and in each simulating
630 all 12 variants. There is a very good correlation between the simulated and calculated lifetimes (d).
631 The mean errors (e; left) are reduced as a function of lifetime, while the standard error between
632 model variants (simulating variability in dye clearance) peaks around the mean dye clearance rate
633 (e; right panel). **f**, Error in the lifetime estimate as a function of the pulse-chase interval (ΔT). The
634 error (blue line) decreases faster than the pulse concentration (black line). **g,** Error in lifetime
635 estimation using only pulse measurements given ideal dye injection delivery. Here, protein
636 expression variability (standard deviation y-axis) could be countered only by averaging between
637 animals (number of animals x-axis). Error rates (color-coded) are higher than in DELTA where
638 the chase dye and the FP calculation normalizes for expression variability.

Extended Data Figure 2 - JF-HTL dyes are cleared from the brain in hours

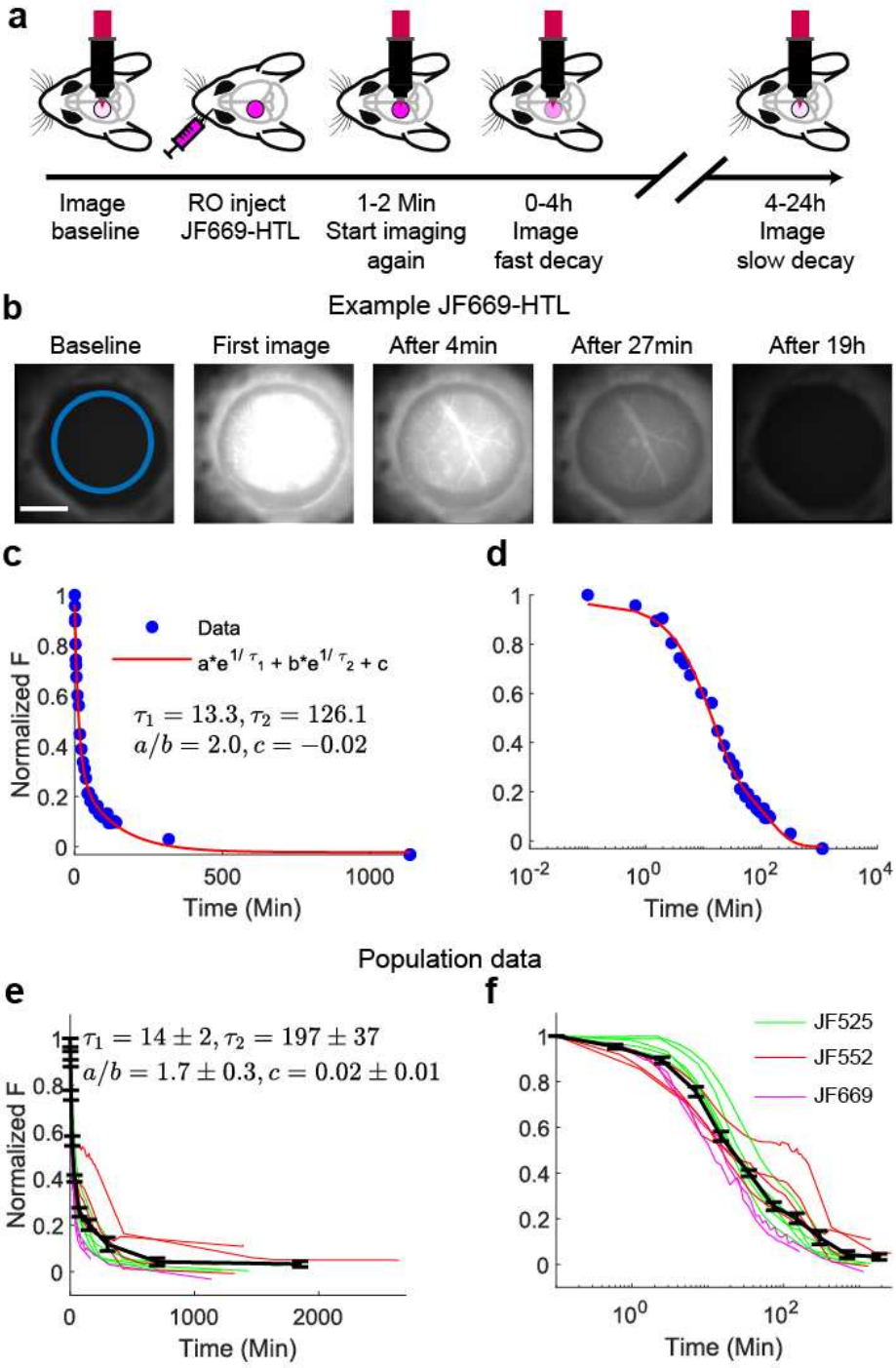

a, Schematic experimental procedure to measure dye clearance. Note that the injection kinetics are not captured as the animal is injected prior to imaging. **b,** Example images for a JF669-

644 HTL injection. The blue circle represents the region for which fluorescence was quantified in c
645 and d. The scale bar is 2mm. **c–d,** Linear (c) and log (d) scale values (peak normalized and baseline
646 subtracted - blue circles) of JF_{669}-HTL dye clearance. Fit to a double exponential fit in red, $\tau 1$ and
647 $\tau 2$ are in minutes. **e-f,** Data from 12 experiments showing clearance of 3 dyes (JF_{525} in green, JF_{552}
648 in red, and JF_{669} in magenta). The black trace is a binned average with standard error of all twelve
649 experiments. The values in E represent the mean ± standard error of double exponential fits for the
650 12 experiments.

651

652

Extended Data Figure 3 – JF_{552} and JF_{669} are bioavailable in the brain

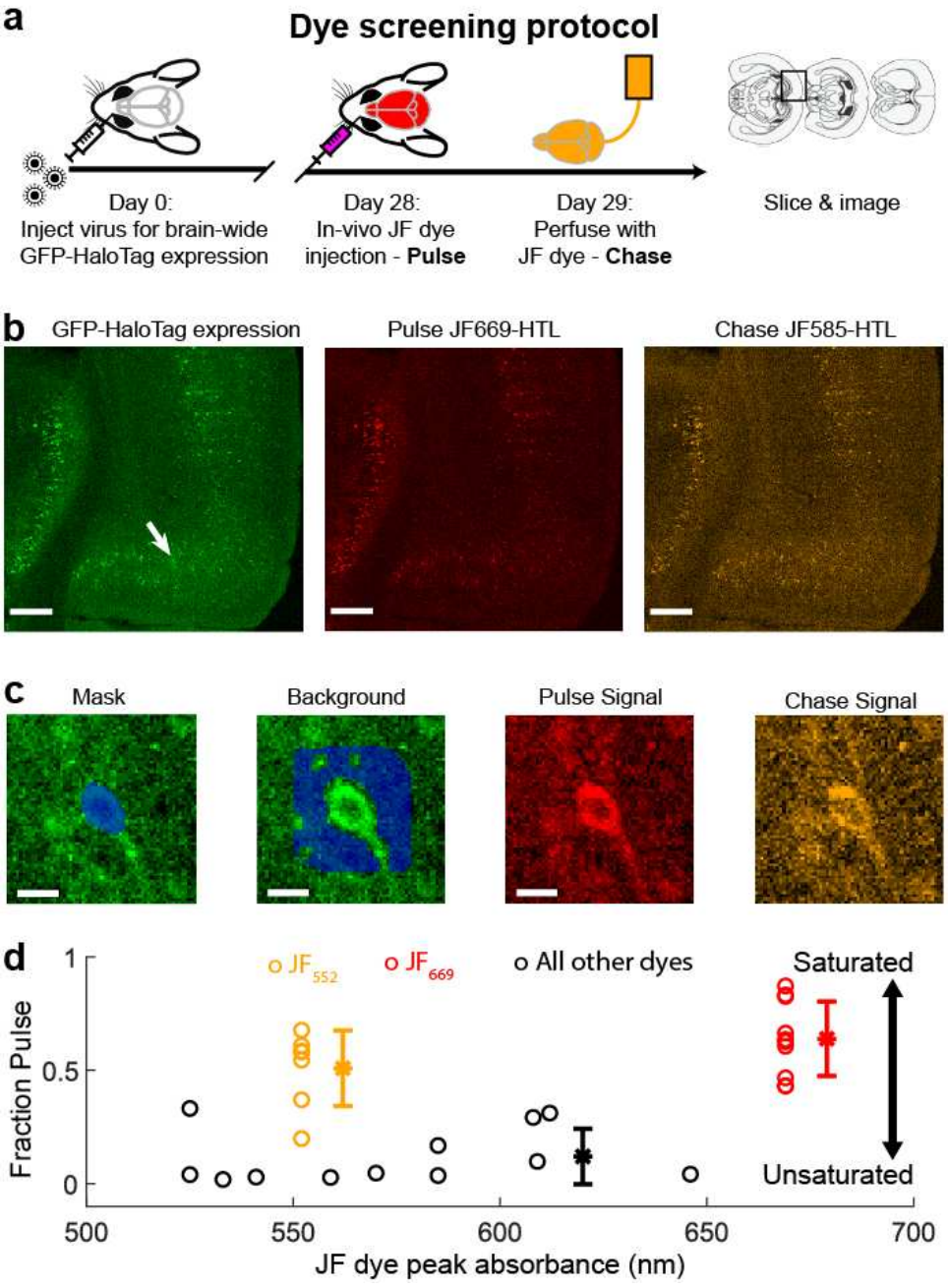

a, Schematic of the experimental procedures for dye screening *in vivo*. **b,** Example coronal sections imaged from an animal 3 weeks after viral injection of GFP-HT (left panel) injected *in vivo* with JF_{669} (middle panel) and perfused with JF_{585}-HTL (right panel). Scale bars, 200 µm . **c,** Example cell (Arrow in B, left panel) overlaid with the mask used to extract signal (first panel), a

660 local background (second panel) and the images of the *in vivo* injected dye (third panel) and
661 perfused dye (fourth panel). FP is 0.65 in this example. Scale bars are 10 µm. **d,** Mean FP for each
662 animal (n=31) injected as a function of the dye excitation wavelength. JF669-HTL (n=10, fraction
663 *in vivo*: 0.64 +- 0.16) is in magenta and JF_{552}-HTL (n=7; fraction *in vivo* 0.51 +- 0.17) in red. Other
664 dyes in black (n=14, 0.12 +- 0.12).

665

Extended Data Figure 4 – Systemic injection of ligand dye saturates the abundant protein MeCP2-HT in most organs

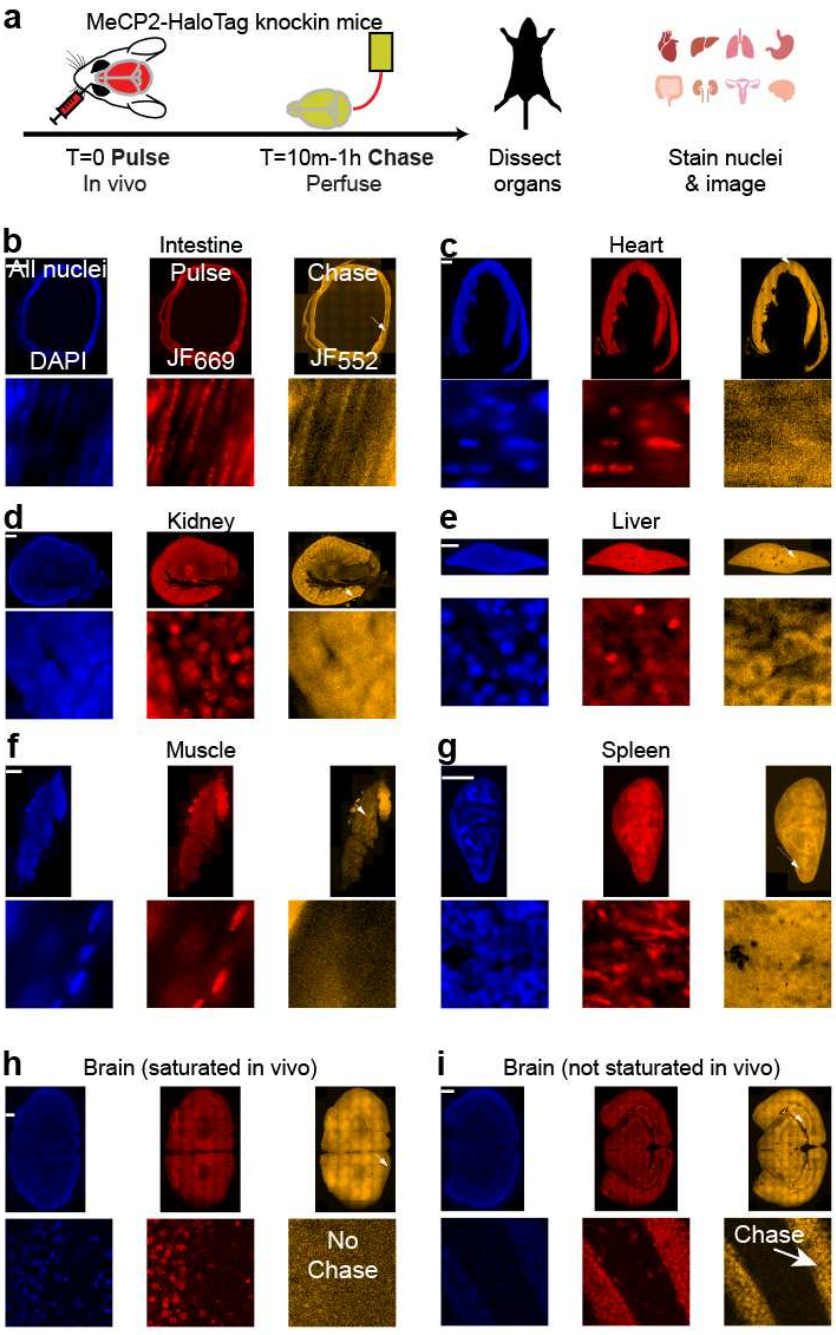

669 **a,** Schematic of the experimental procedures to test the saturation of MeCP2-HT. **b-i,** Organs
670 harvested and imaged for pulse dye saturation (red), as evident by the lack of chase dye (orange)
671 in the nuclei (blue) where MeCP2-HT is expressed.

Extended Data Figure 5 - The lifetime of MeCP2-HT is consistent between individual mice and cell-types

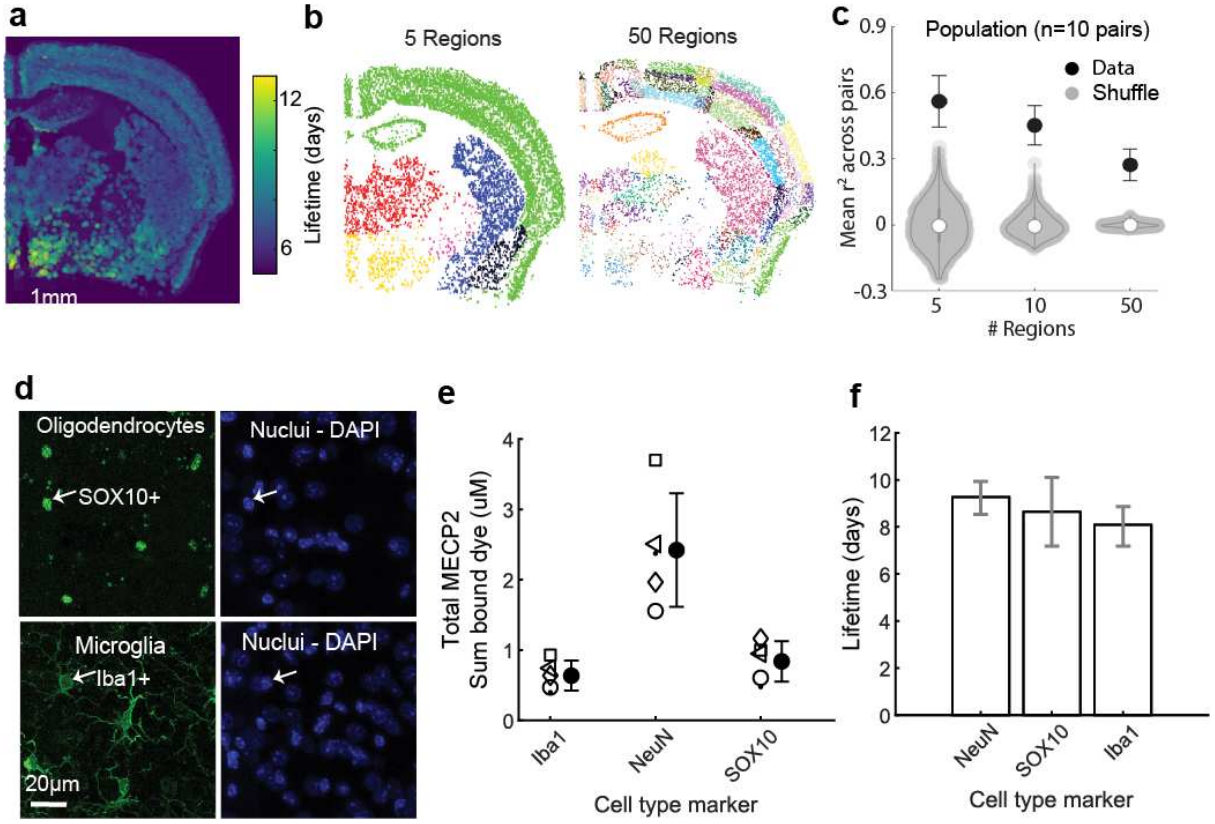

a, Example coronal section of the lifetime of MeCP2-HT after segmentation of neuronal positive nuclei. **b,** Example assignment of nuclei to brain regions based on CCF at different levels (left 5 regions, right 50 regions). **c,** Protein lifetime measurements were consistent between mice as assessed by looking at pairwise correlations between all possible pairs of animals (n=5 animals, 10 pairs). For each level of the CCF (5, 10, and 50 regions) the correlation between regions was higher than for a shuffled control. **d,** Two additional sections were stained in each of the five animals for oligodendrocytes (SOX10, top) and microglia (Iba1, bottom). **e,** MeCP2 was more abundant in the nuclei of neurons (Iba1: 0.63±0.21, NeuN: 2.42±0.8 SOX10: 0.84±0.28 µM total dye signal; ANOVA F=27.22, df=2, p=2e-4). **f,** Lifetimes were similar for all cell types, since confidence intervals overlapped between all cell types (mean [CI] of Iba1: 9.2 [8.5, 9.9], NeuN: 8.6 [7.1 10.0], SOX10: 8.1 [7.2, 8.9] days of MeCP2 lifetime).

Extended Data Fig. 6 – Development of JFX_{673}-HTL for optimal *in vivo* dye delivery

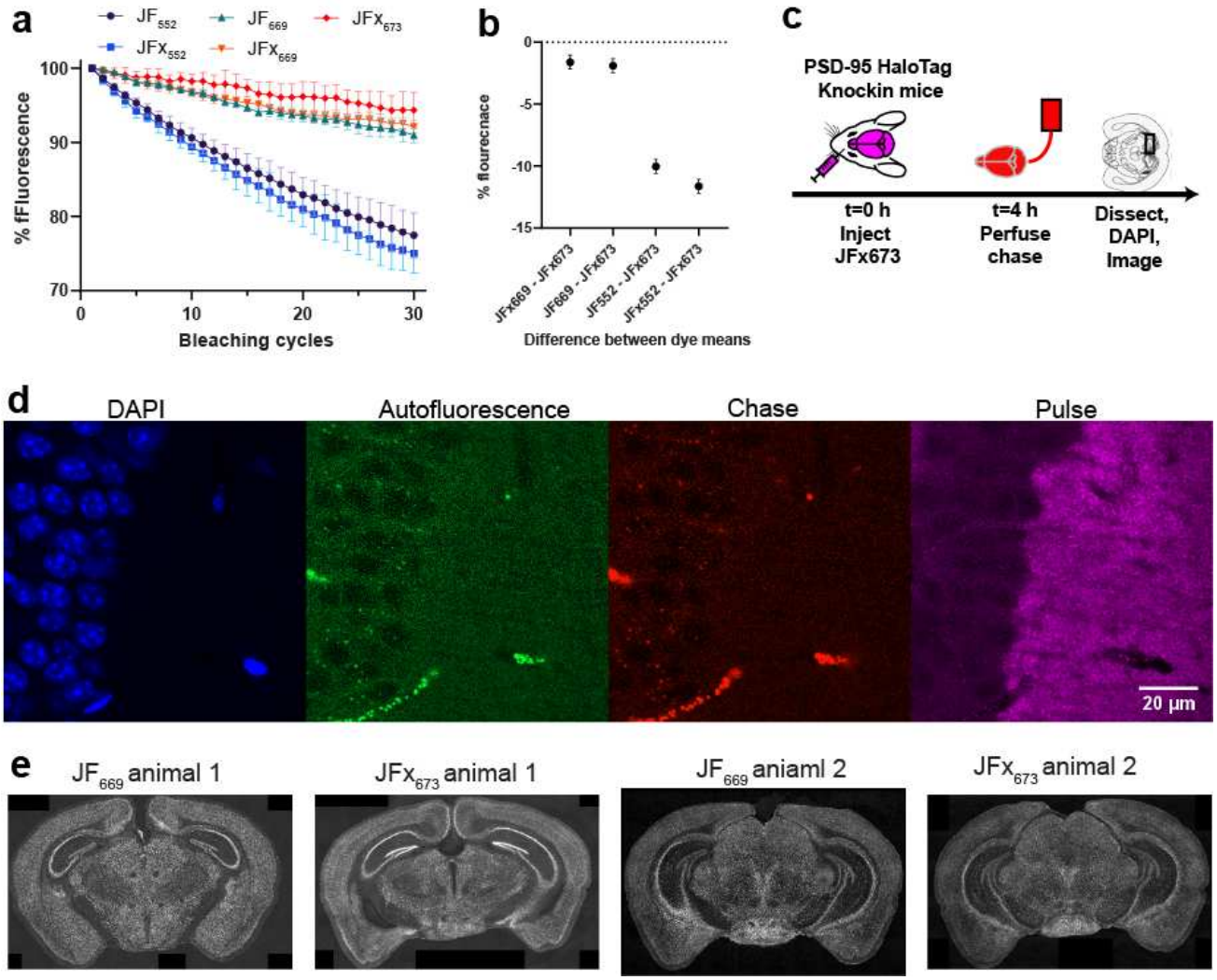

a, Bleaching curves of JF dyes showing normalized fluorescence over 30 bleaching cycles. **b,** JFX_{673}-HTL was significantly more photostable than the other dyes tested. **c,** Experimental procedures for testing saturation in a PSD95-HT mouse. **d,** Example section of the animal in (c) showing the basal dendrite section of the CA1 region of the hippocampus (DAPI shows the nuclei in the leftmost panel). The autofluorescence seen in the green channel (2^{nd} panel from left) explains all the fluorescence in the chase channel (JF_{552}-HTL; 3^{rd} panel), while the far-red channel shows the expected pattern of synapses (JFX_{673}-HTL; 4^{th} panel). **e,** Example sections of MeCP2-HT mice do not show significant differences in brain availability of JF669-HTL versus JFX_{673}-HTL.

Supplementary note 1: Simulations of pulse-chase experiments

To understand the conditions under which DELTA would provide accurate measurements of protein lifetime, we turned to simulations. We investigated possible sources of error, including dye pharmacokinetics, amount of dye injected, variability in dye clearance, and pulse-chase interval (ΔT). While the dye amount and ΔT are experimentally controlled, a crucial unknown is the pharmacokinetics of the HaloTag ligand (HTL) dyes. For example, if the free HTL dye is not cleared quickly, new HT-protein could be labeled by the pulse dye instead of the chase dye, thus biasing the measurement to longer lifetimes.

We first measured the rate of dye clearance in the brains of wild-type mice. HTL JF dyes were injected into the retroorbital sinus (**Extended Data Figure 2a; Methods**)[59] and imaging was subsequently performed with a wide-field fluorescence microscope[58] through a cranial glass window[60,61], for up to 24 hours after injection (**Extended Data Fig. 2b** for example imaging session). Dye concentration decayed with a dominant fast component (14±2 min), in addition to a slower component (197±37 min; **Extended Data Fig. 2c-d** and **Supplementary Table 1**; fast/slow ratio: 1.7±0.3; n=12; corresponding to a geometric average dye lifetime of 82 min). We incorporated dye clearance kinetics into our model (**Extended Data Fig. 1a**). Dye in a "Brain" compartment could either bind to the free protein-HT, directly clear out (corresponding to the fast component), or partition into a second compartment ("Lipids" corresponding to the slow component). As we measured dye clearance 12 times, and it had some variability in its clearance kinetics, we could fit model parameters to each *in vivo* dye clearance experiment's data (**Extended Data Fig. 1b**). This leads to 12 model variants that are different in the three parameters that impact dye clearance kinetics (Lipids compartment volume, fast clearance rate constant, and Brain to Lipids equilibrium constant).

Because each HT-protein exists at different concentrations *in vivo*, it is difficult to inject the precise amount of HTL JF dye to saturate the HT-protein. Should we aim to under-saturate or provide dye excess? To address this question, we varied the ratio of dye to protein-HT target and estimated the error in estimating protein turnover for a broad range of average protein lifetimes (**Fig. 1b**). The dependence of the error on protein lifetime has three regimes. First, under saturated

727 labeling (**Fig. 1b** - dye/protein ratio < 1) has large errors regardless of protein lifetime. Second is
728 dye saturating (**Fig. 1b** - dye/protein ratio > 1) where the protein lifetime is short, and the errors
729 are large and mirror the under-saturating regime. Third, where we have both dye saturation and
730 long protein lifetime (>40h), here error is quite small. The main factor contributing to this effect
731 in the dye saturating regime is the time of dye clearance relative to the measurement time. As the
732 dye clears in an hour (**Extended Data Fig. 2**), the relative contribution to the error increases for
733 shorter lived proteins, which entail shorter pulse-chase intervals. Specifically, in the saturating
734 regime (>1.2 dye/protein ratio), dye clearance kinetics would bias the lifetime estimate towards
735 longer lifetimes, as slower dye clearance delays the onset of unlabeled protein production (see
736 arrow in **Fig. 1a**). This would increase P at the expense of C and would inflate the lifetime
737 estimation. In a noncomplete saturation regime (1-1.2 dye/protein ratio) during dye injection, more
738 protein is made for shorter-lived proteins, thus more dye is consumed during the dye clearing
739 window, this reduces the error introduced by dye excess. These competing factors create a
740 nonmonotonic relationship between the estimation error and the protein lifetime (**Extended Data**
741 **Fig. 1e**). Thus, two of the necessary conditions for reliably measuring the protein lifetime using
742 DELTA is saturation of the target protein with pulse dye injection while avoiding very short-lived
743 proteins. This is not very limiting as even immediate early gene proteins have hours long lifetimes[2].

744 We next measured the effect of model variants (combination of the Lipids compartment
745 volume, fast dye clearance rate, and Brain to Lipids equilibrium constant) on the estimation of
746 protein lifetime across a wide range of simulated lifetimes (**Extended Data Fig. 1c**). These
747 variants capture the uncontrolled variable corresponding to the variance in dye clearance that
748 would lead to variance (not bias) in our measurements. Using a pulse-chase interval equal to the
749 average protein lifetime ($\Delta T = \tau$) and a pulse dye amount in the saturating regime (1.2 dye/protein
750 ratio), we compared the estimated lifetime with the true one and found a good correspondence
751 (**Extended Data Fig. 1d**; r^2=0.9996 n=84, 12 variants × 6 lifetimes). We noticed a nonmonotonic
752 relationship between bias and protein lifetime (Mean of error as defined above; **Extended Data**
753 **Fig. 1e –** left panel), as expected from the single-model variant simulation. Of note, while bias
754 would lead to an overestimation of the lifetime, it does not affect our ability to make comparisons
755 between brain regions in the same animal or between animals. Dye injection variability (Standard
756 deviation of Error; **Extended Data Fig. 1e** – right) would affect our ability to compare the lifetime

and has a nonmonotonic shape as well. However, in all cases these were small (less than 5%). We then turn to estimating the effects of the pulse-chase interval (T) on the lifetime estimation error. While the protein decayed exponentially (**Extended Data Fig. 1f** – green line), error decreased faster as function of ΔT (**Extended Data Fig. 1f** – red line). This decay of error again supported the idea that the main bias in this measurement is the relative time of dye clearance.

Last, we used modeling to compared our pulse-chase method to measurements using pulse only[30]. Here, we assumed the same lifetime (100 h), a perfect measurement of the pulse, and the only variability would come from the expression of the protein. We assumed that different animals would have on average 1 AU and varied the width of the distribution (uniform from ±0.05 to ±0.45 AU; **Extended Data Fig. 1g** – y axis). The range was selected conservatively according to the values seen in mass spectroscopy (MS) for biological replicates. That is, the variability of the amount of protein between animals[62,63]. This variability could be reduced by averaging over multiple animals. We calculated the error in estimating the lifetime as a function of the number of animals used (**Extended Data Fig. 1g – x axis;** 4-72). These were distributed over four time points (0, 10, 30, 100h) in which a single exponential decay was fitted after averaging across animals (average #animals per time point of 1, 3, 6, 12 animals). The estimation error increased with increasing protein expression variability and decreased with averaging over animals, as expected. However, for most operating regimes of DELTA, there would be no error under these conditions, as the fraction pulse calculation normalizes for the total protein amount.

Supplementary note 2: Screening for bioavailable JF dyes

We screened HaloTag ligand (HTL) dyes that would be able to saturate abundant proteins in the brains of mice by measuring bioavailability in the brain (**Extended Data Fig. 3**). Our target was a green fluorescent protein tagged with HT (GFP-HT). AAV-PHP.eB expressing GFP-HT was introduced by retroorbital injection[64], which led to sparse and brain-wide expression (**Extended Data Fig. 3a, Supplementary Figs. 1,2**). Four weeks after viral transduction, HTL dyes (**Supplementary Table 2**) were injected retroorbitally (Methods; **Supplementary Note 3**).

After 12-18 hours, we perfused the brain with a spectrally orthogonal dye. Given that GFP has a lifetime of several days[65], FP is a measure of the dye's ability to saturate the protein-HT target.

The brain was sectioned coronally and imaged with a confocal slide scanner (methods). Example images from an injection show the target protein in green (**Extended Data Fig. 3b**, left panel), the *in vivo* delivered dye in red (JF_{669}-HTL; **Extended Data Fig. 3b**, middle panel) and perfusion dye (JF_{585}-HTL; **Extended Data Fig. 3b**, right panel) in orange (**Supplementary Fig. 1** for more example injections). This procedure enabled analysis of single cells (**Methods**; **Extended Data Fig. 3c**). The fluorescence values of individual cells were background corrected and converted to dye concentration using calibration curves (**Supplementary Fig. 3a**). These calibrations are needed to determine the total protein amount (P + C) correctly as the illumination and detection sensitivities of the dyes vary.

We identified two dyes that saturated GFP-HT in the brain: JF_{669}-HTL (n=10, FP: 0.64 +- 0.16) and JF_{552}-HTL (n=7; FP: 0.51 +- 0.17)> These dyes were significantly better than the other dyes tested (**Extended Data Fig. 3d** 1-way ANOVA F=35.96, df=2, p =3.2e-08; post-hoc JF_{669} vs. Others p=3.8e-8, JF_{552} vs. others p=2.7e-5). Variability in GFP-HT expression did not account for the variability in these dyes, as the number of detected cells or virus signals did not correlate with FP (**Supplementary Fig. 3b-c**; Virus signal correlation: r^2=0.02, p=0.45, n=28; #cells correlation: r^2=0.005, p=0.717, n=28). Another check we can do is to look at the correlation between FP and the GFP/P ratio. We expect that a higher FP would correlate with a higher P/GFP ratio. Here, a large difference would implicate issues with the perfusion and complete saturation of the GFP-HT target with the chase. However, FP did correlate with the P/GFP ration as expected if the perfusion dye saturates the remaining GFP-HT proteins (**Supplementary Fig. 3d**).

We next quantified the amount of variability across brain regions in the delivery of the dye under these under-saturation conditions. We therefore looked at individual cells along all coronal sections imaged (examples in **Supplementary Figures 2a, b**). These injections produced low variability along the AP axis (**Supplementary Fig. 2c**) as indicated by normalizing the average FP in the front of the brain and the lack of any trend toward the back of the brain (**Supplementary Fig. 2d**). Looking at individual coronal sections (**Supplementary Fig. 2e**), we see a low CV for each slice for our bioavailable dyes (**Supplementary Fig. 2f**). This indicates low variability in dye

delivery across the brain for JF_{669}-HTL and JF552-HTL, which would help uncover variability in protein lifetime across brain regions.

Supplementary note 3: Injection and formulation for bioavailability of JF dyes

JF-HTL dyes are a key reagent for DELTA. We characterize JF-HTL dyes in terms of infusion kinetics, formulation, solubility, and the brain's reaction in terms of inflammation. We first wanted to understand whether the injection rate can affect the dye's ability to saturate proteins in the brain. However, due to the retroorbital injection procedure, we were unable to capture the dye dynamics during injection as the mouse headbar physically interfered with the retroorbital injection. Additionally, it is difficult to precisely control the rate of delivery in retroorbital injections, as they are performed manually. To perform these types of experiments we needed a precise i.v. dye delivery method that would enable simultaneous brain imaging. We choose to use carotid artery perfusion to deliver JF_{669}-HTL at different rates during continuous imaging through a cranial window (Methods; **Supplementary Fig. 4a**). In these experiments, if doubling the rate of dye delivery exactly doubles the rate of dye increase in the brain, this would indicate that the dye clearance is linearly proportional to the dye injection rate. This would tell us that the dynamics of dye injection would not dramatically change the total amount of dye delivered to the brain. However, if the slope of dye accumulation in the brain increases more than twofold, it would indicate a saturation of the dye clearance mechanism. This would favor faster dye injections leading to higher peak concentrations and total dye delivery to the brain. In the first mouse (**Supplementary Fig. 4b**) we perfused dye at 20ul/min (**Supplementary Movie 1**) and 40ul/min (**Supplementary Movie 2**) and observed a more than twofold increase in the slope of dye accumulation in the brain (1.9 to 6.3 AU/min). We repeated this experiment with another animal (**Supplementary Fig. 4c**) and saw similar over two-fold increases in slope (**Supplementary Fig. 4d**). We validated our intuition about the effects of a constant clearing rate using simulations (methods). Using the same amount of dye (20AU) and a constant clearance rate (1AU/dt), we simulated different injection rates (2-10AU/dt). We observed saturation further away from the injection center for faster injection rates (**Supplementary Fig. 4e**). These results favor an injection method that delivers the dye faster given a constrained amount of dye.

To understand our dye constraints, we checked the dye solubility. We validated that our JF-HTL dyes are soluble at our desired concentration (1mM; **Methods**) and stable over time. We used the published formulation for injection[58] adding 20ul DMSO, 20ul Pluronic F127 and 60ul PBS. If we are near the solubility limit, the amount of dye post-resuspension would decrease. This was not the case for all dyes injected *in vivo* (**Supplementary Fig. 5a**; 2way ANOV [Dye x Time] $p<0.05$; Time: $F = 0.66$, DFn=3, DFd=20, $p=0.5835$; Dye: $F=149.21$, DFn=4, DFd=20, $p<0.0001$; Interaction: $F=1$, DFn=12, DFd=20, $p=0.4794$). The only dye that did not reach our solubility goal was JF585-HTL and was not used *in vivo*. It was used during perfusion at a much lower concentration (1uM) well below the solubility limit (~250uM).

We then wanted to know if the ratio of DMSO to Pluronic F127 (1:1 or 20ul/20ul) was optimal for dye availability. We tested both increasing and reducing the ratio, but the original ratio was the best (**Supplementary Fig. 5b**). As we were injecting 40-80ul (~2-4g/kg) of DMSO which is lower than the LD50 (>10g/kg)[66] but not a small amount. We tried to replace DMSO with Captisol as cosolvent and evaluated both the solubility and the in vivo injections. We saw mixed effects of dyes and formulations by looking at solubility after a 3-day incubation with DMSO, Captisol and a combination of Pluronic F127 and Captisol (**Supplementary Fig. 5c**; 2-way ANOVA, interaction: $F = 13.31$. DFn = 6, $p<0.0001$; Dye: $F = 67.35$. DFn = 3, $p<0.0001$; Formulation: $F = 46.91$. DFn=2, $p<0.0001$). We tested both JF669 and JFx673 using retroorbital injections with the different formulations. As expected from the solubility data, JF669 in other formulations was less bioavailable (**Supplementary Fig. 5d** – left column). However, although JFx_{673} was soluble in all formulations, it was still less bioavailable in the brain using Captisol (**Supplementary Fig. 5d** – Right column).

Lastly, we validated that there were no signs of brain inflammation using GFAP and Iba1 markers that we validated with a cortically lesioned animal (**Supplementary Fig. 5e -** panel i) and a naïve animal (**Supplementary Fig. 5e -** panel ii). Both retro-orbital virus injections (**Supplementary Fig. 5e -** panel iii) and our chosen dye injection formulation (**Supplementary Fig. 5e -** panel iv) were as the naïve animal. This indicates that there is no major breach of the brain blood barrier, as it is known to induce this type of inflammation[67].

Supplementary Figures

Supplementary Figure 1 – Additional raw data from dye screening

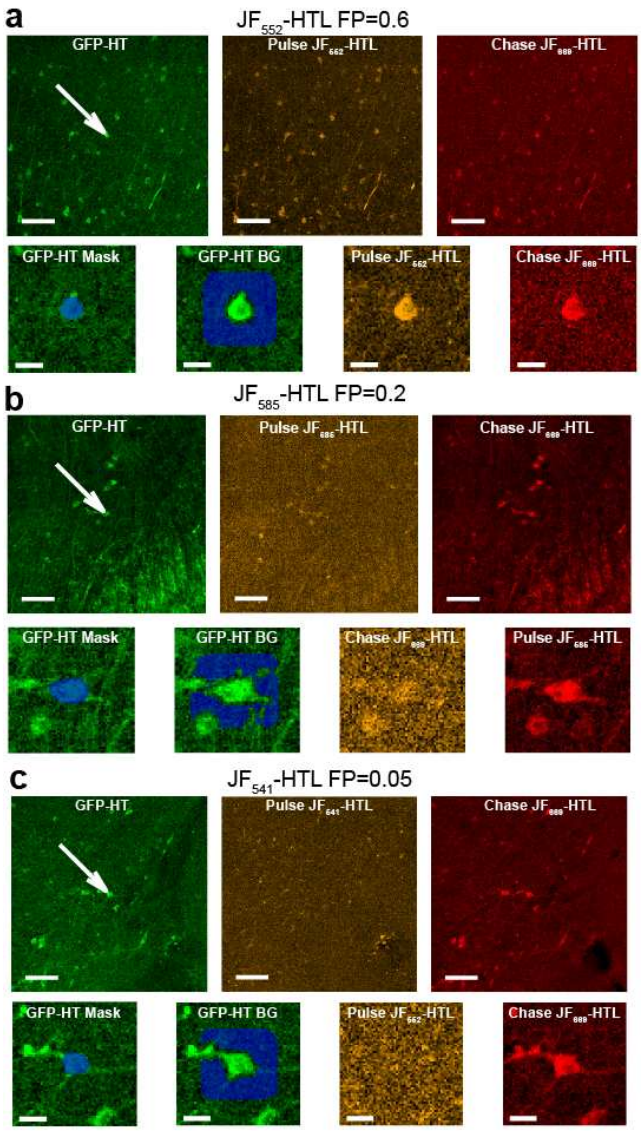

a, Example coronal section imaged from an animal 3 weeks after viral injection of GFP-HT (top left panel) injected *in vivo* with JF552-HTL (top middle panel) and perfused with JF669-HTL (top right panel). The bottom panels show an example cell (Arrow in the top left panel) overlaid with the mask used to extract signal (first bottom panel), a local background (second bottom panel), and images of the *in vivo* injected dye (third bottom panel) and perfused dye (fourth bottom panel).

880 FP is 0.6 in this example. **b,** same as (a) for JF_{585}-HTL with FP=0.2. **c,** same as (a) for JF_{541}-HTL
881 with FP=0.05.

882 Supplementary Figure 2 – Brain dye capture was uniform across
883 the brain

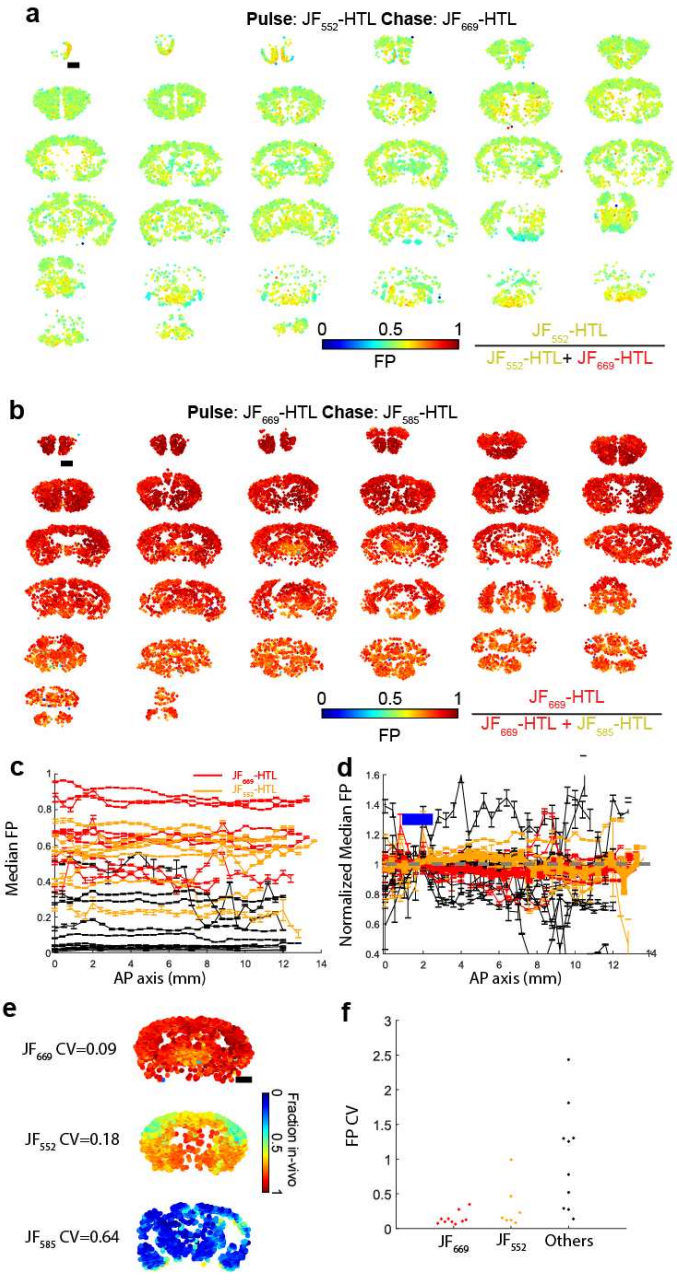

884

a, Coronal slices of GFP-HT injected mouse brain after JF_{552}-HTL dye injections. Each dot is a cell colored by FP. The scale bar is 1mm. **b,** same as (a) for JF_{669}-HTL **c,** Median FP as a function of AP position (of coronal slices). JF_{669}-HTL is in red and JF552 is in orange. Error bars are standard errors. **d,** After normalization (Mean of the median fraction in vivo under the blue line is set to 1), there is no significant deviation from 1 suggesting uniformity of dye distribution in this axis (One-way ANOVA, df =19, F=1.46, p=0.0913). **e,** For each coronal section of each animal, a coefficient of variation (CV) was calculated. Three examples of coronal sections are shown. **F,** CV of FP for JF_{669}-HTL injections (Red, CV=0.15±0.03, n=10), JF_{552}-HTL (Orange, CV=0.31±0.12, n=7) and the other dyes (Black, CV=2.2±0.81, n=14).

Supplementary Figure 3 – Calibration and validation of GFP-HT based JF dye screening *in vivo*

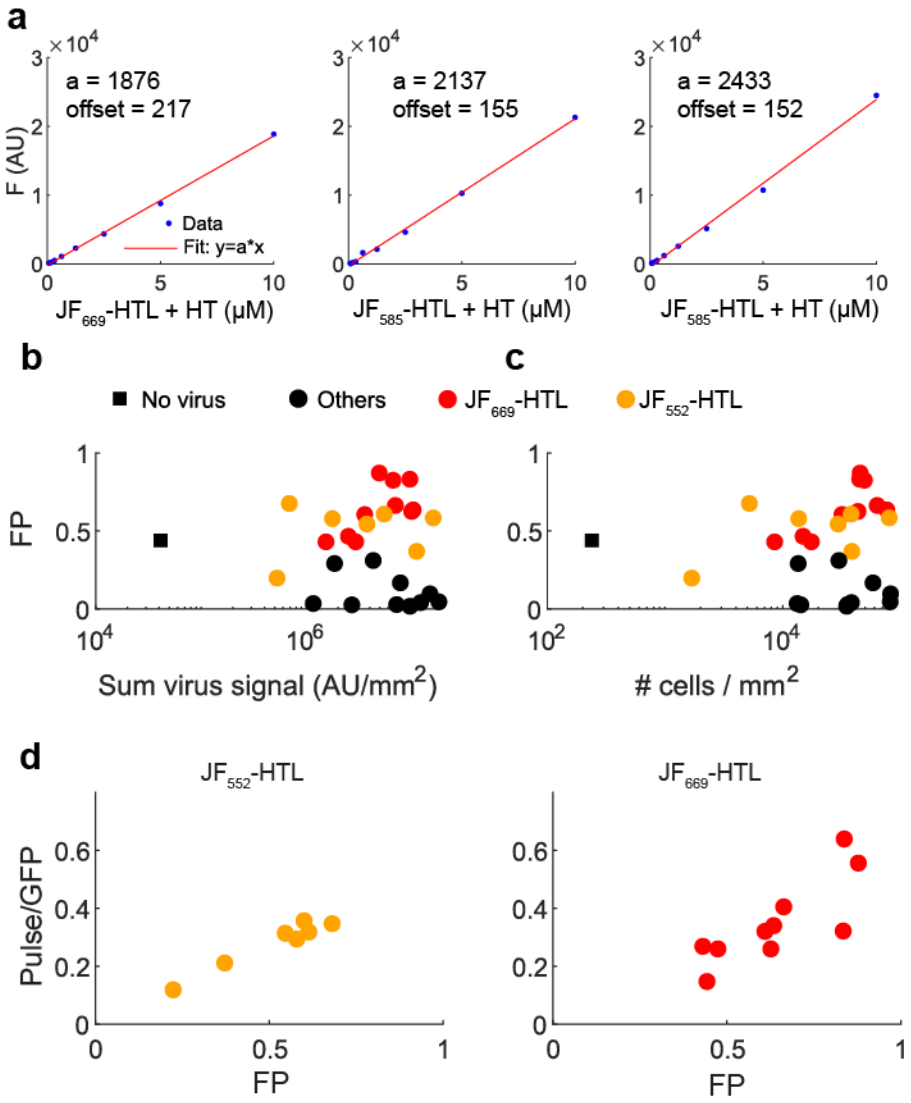

a, Purified HT was added at saturation to a HTL JF dye (left:JF_{669}-HTL, middle:JF_{585}-HTL, right:JF_{552}-HTL) in a 8 well coverslip wells at 20 µL/well with the following concentrations (µm): 10, 5, 2.5, 1.25, 0.625, 0.3125, 0.15625, 0. All 8 wells were imaged under the same conditions as the fixed tissue slides (far red channel for JF_{669} and red channel for JF_{552} and JF_{585}). The offset at zero was subtracted and is reported in each panel. A linear slope (a-red line) was fitted to the data (blue circles) without an intercept term (JF_{669}-HTL: R^2=0.998; JF_{585}-HTL: R^2=0.9982; JF_{552}-HTL R^2=0.9963). This calibration covers 20 out of the 30 animals used and a naive calibration was used

for the rest of the dyes (150 offset, 2000 slope). **b,** Mean fraction in vivo is not correlated with the sum of the virus signal per animal (Magenta is JF_{669}-HTL, red is JF_{552}-HTL, black is other dyes). An animal that was not injected with a virus (Black square) has at least an order of magnitude less summed fluorescence (r^2=0.02, p=0.45, n=28). **c,** Mean fraction in vivo is not correlated with the number of cells detected per animal (normalized by the area of tissue imaged). An animal that was not injected with a virus (Black square) has at least an order of magnitude less detected cells (r^2=0.005, p=0.717, n=28). **d,** As the FP increases, so is the ratio between the pulse dye and GFP, indicating that variability in the chase cannot explain the increases in FP (JF_{552}-HTL:N=7, df=5 R^2=0.945, F=85.5, p=0.00025; JF_{669}-HTL: N=10, df=8, R^2=0.65, F=14.7, p=0.00495).

Supplementary Figure 4 – Injection pharmacokinetics of JF dyes

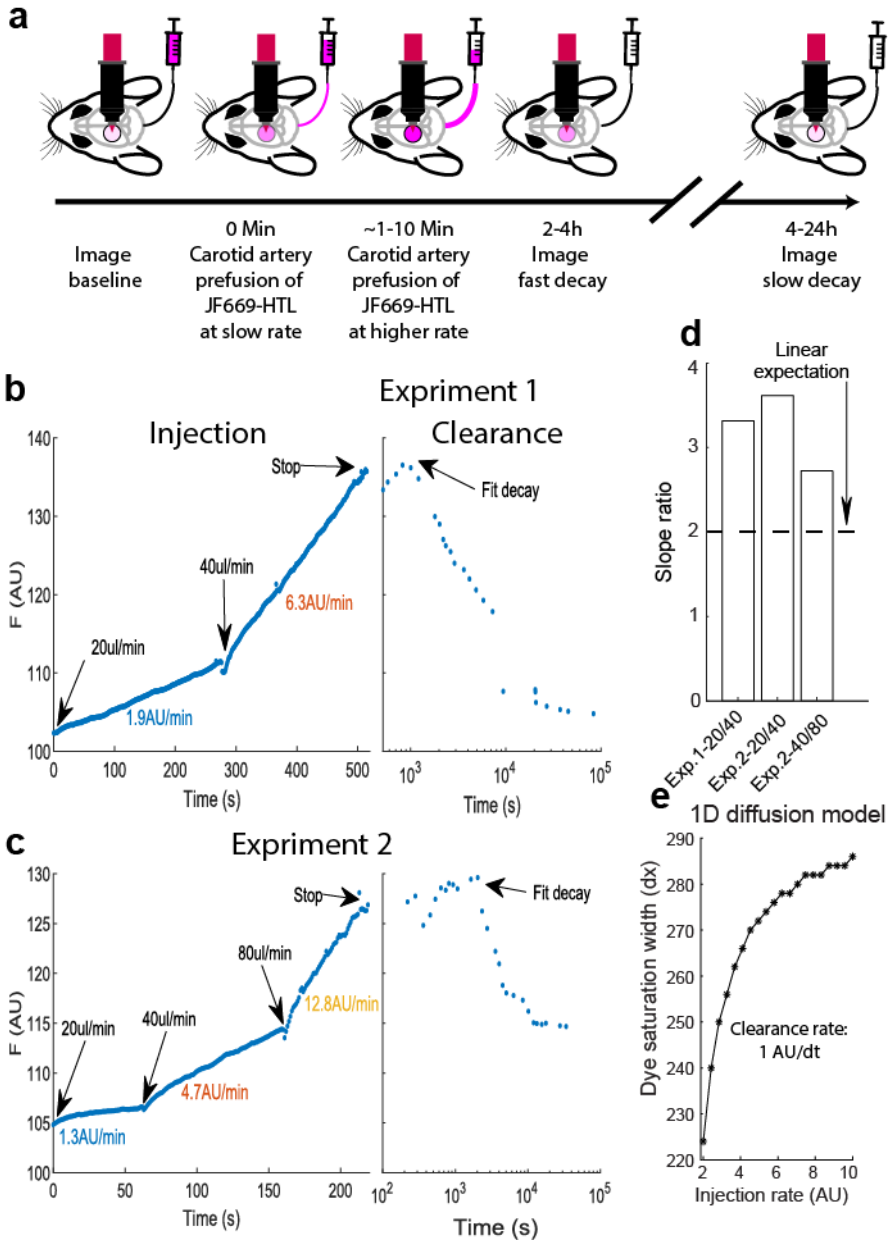

a, Design of experiment to measure dye injection pharmacokinetics. Continues imaging was performed during carotid artery perfusion of JF_{669}-HTL at different rates. **b,** Experiment 1 in which 20 µl/min and 40 µl/min infusion rates were used. **c,** Same s (b) but with another animal with 20, 40 and 80 µl/min infusion rates. **d,** Slope ratios for all transitions in infusion rates. If clearance was proportional to the amount of dye injected, a slope ratio of 2 is expected. A slope ratio of > 2

implies sublinear clearance or saturation of clearance mechanisms. **e,** 1D diffusion model shows an increase in the area of saturation (y-axis) with increasing dye injection rate (x-axis).

Supplementary Figure 5 - Effects of JF dye formulation on bioavailability and solubility

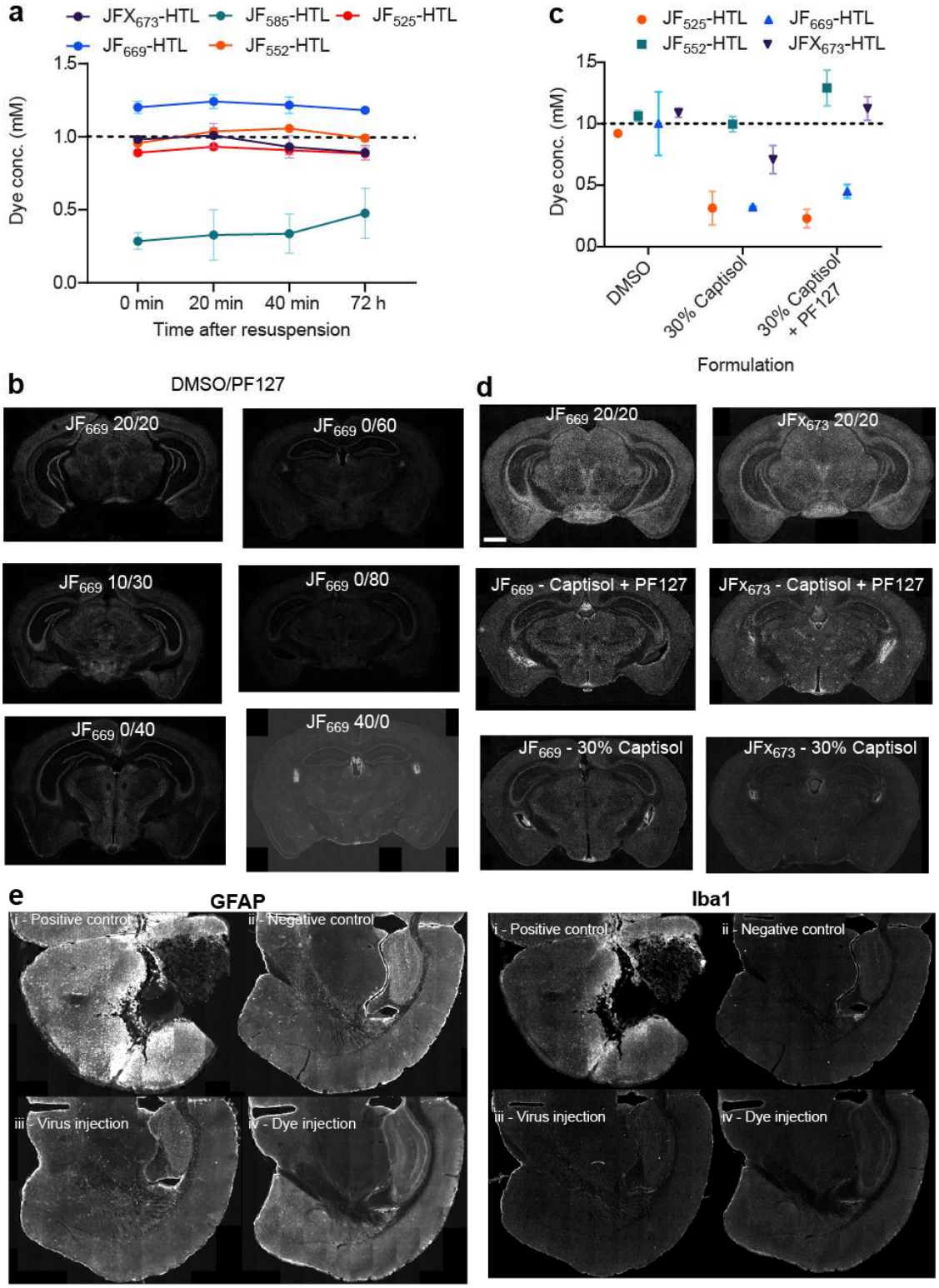

928 **a**, Solubility of JF-HTL dyes using DMSO (20ul) Pluronic F127 (20ul) and PBS (60ul)
929 formulation over time. No significant decrease in solubility was observed and all *in vivo* dyes used
930 reached the intended solubility of 1mM **b,** Example coronal slices from MeCP2-HT animals
931 injected with different ratios of DMSO and Pluronic F127. The original 1:1 ratio was the best, as
932 shown by the brighter pulse dye staining. **c,** Different formulation then (a) to test the replacement
933 of DMSO (left) with Captisol (middle) or a combination of Captisol and Pluronic F127 (right). We
934 saw mixed effects on solubility, while some dyes retained (JFX_{673}-HTL) solubility, and some did
935 not (JF_{669}-HTL). **d,** Example coronal slices from MeCP2-HT animals injected with solutions from
936 (c). Both dyes that were less soluble with Captisol/Captisol and Pluronic F127 (JF669 left) or those
937 that were as soluble (JF673 right) were less bioavailable without DMSO. **e,** Immunohistochemistry
938 against GFAP (left) and Iba1(right) for 4 conditions, i-positive control: a cortical lesion. ii-
939 Negative control: Naive animal without any manipulation. iii-Virus injection: An animal was
940 injected with the GFP-HT virus and perfused 3 weeks after injection. iv-Dye injection: An animal
941 was injected with JF_{669}-HTL and perfused 24 h after injection. Both dye injection and virus
942 injection do not increase GFAP or Iba1 levels.

943

944 Supplementary Table 1 – Animals and filters used for dye
945 clearance experiments

ID	Date	Animal#	JF Dye	Obj.	Light source	Window
1	2019-03-22	444570	525	16x	1.5A Mightex 525	ALM
2	2019-03-25	439476	525	4x	1.5A Mightex 525	ALM
3	2019-03-26	439476	525	4x	1.5A Mightex 525	ALM
4	2019-03-28	434848	525	4x	3A Mightex 525	V1
5	2019-05-14	434848	552	20x	100% 565 coolLED	V1
6	2019-07-16	452088	669	4x	X-Cite 120	ALM
7	2019-07-17	452088	552	4x	5A Mightex 525	ALM
8	2019-07-18	452088	669	4x	X-Cite 120	ALM
9	2019-07-19	454527	552	20x	5A Mightex 525	ALM
10	2019-07-20	454814	669	4x	X-Cite 120	ALM
11	2019-07-22	452932	525	20x	5A Mightex 525	ALM

946

947

Supplementary Table 2: Animals and dyes used for ex vivo screening

Batch	Animal number	DOB	Virus injection date	HT-Expression	Dye injection	In-vivo dye	DMSO/PF127/ Saline/Injection (µl)	Chase dye	Mount	Fraction *in vivo*
2	439359	8/14/18	11/26/18	GFP	1/3/19	JF669	20/20/200/200	JF585	5th	0.47
2	439360	8/14/18	11/26/18	GFP	1/3/19	JF669	20/20/400/200	JF585	5th	0.43
3	444182	10/16/18	1/3/19	GFP	2/5/19	None	virus only	None	1	hist.
3	444185	10/16/18	1/3/19	GFP	2/5/19	JF585	30/10/200/200	JF669	5th	0.04
3	444186	10/16/18	1/3/19	GFP	2/5/19	JF585	10/30/200/200	JF669	5th	0.17
5	447231	12/4/18	4/5/19	GFP	5/1/19	JF669	20/20/200/200	JF585	4th	0.64
5	447232	12/4/18	4/5/19	GFP	5/1/19	JF669 2x	20/20/200/200	JF585	4th	0.66
5	447233	12/4/18	4/5/19	GFP	5/1/19	JF669 2x	20/20/200/200	JF585	4th	0.61
5	447234	12/4/18	4/5/19	GFP	5/1/19	JF669	10/30/200/200	JF585	4th	0.82
5	447235	12/4/18	4/5/19	GFP	5/1/19	JF669	10/30/200/200	JF585	4th	0.43
6	445766	12/5/18	4/12/19	GFP	5/8/19	JF552 2x	20/20/200/200	JF669	4th	0.54
6	445767	12/5/18	4/12/19	GFP	5/8/19	JF552 2x	20/20/200/200	JF669	4th	0.58
6	445768	12/5/18	4/12/19	GFP	5/8/19	JF552	20/20/200/200	JF669	4th	0.68
6	447239	12/4/18	4/12/19	None	5/8/19	JF552	20/20/200/200	JF669	4th	hist.
6	447240	12/4/18	4/12/19	GFP	5/8/19	JF552 2x	20/20/200/200	JF669	4th	0.61
7	452036	2/19/19	4/19/19	GFP	5/18/19	JF541	20/20/200/200	JF669	24th	0.03
7	452037	2/19/19	4/19/19	GFP	5/18/19	JF559	20/20/200/200	JF669	24th	0.03
7	452038	2/19/19	4/19/19	GFP	5/18/19	JF533	20/20/200/200	JF669	24th	0.02
7	452039	2/19/19	4/19/19	GFP	5/18/19	JF552	20/20/200/200	JF669	4th	0.37
8	452031	2/19/19	4/26/19	GFP	5/22/19	JF669	20/20/200/200	JF585	4th	0.87
8	452032	2/19/19	4/26/19	GFP	5/22/19	JFX612	20/20/200/200	JF585	4th	0.31
8	452033	2/19/19	4/26/19	GFP	5/22/19	552	20/20/200/200	JF669	4th	0.58
8	452034	2/19/19	4/26/19	GFP	5/22/19	608	20/20/200/200	JF552	4th	0.29
8	452035	2/19/19	4/26/19	GFP	5/22/19	Jfx608	20/20/200/200	JF552	4th	0.1
10	451116	3/11/19	7/15/19	mKate2	8/12/19	525	20/20/200/200	JF669	4th	0.33
10	451119	3/11/19	7/15/19	mKate2	8/12/19	525	20/20/200/200	JF669	4th	0.04
11	458564	5/21/19	8/8/19	GFP	11/11/19	JF669	20/20/200/200	JF585	4th	0.83
11	458565	5/21/19	8/8/19	GFP	10/24/19	JF669	20/20/200/200	JF552	4th	0.63
11	458566	5/21/19	8/8/19	GFP	10/24/19	JF646Bio	20/20/200/200	JF552	4th	0.04
11	458567	5/21/19	8/8/19	GFP	11/11/19	JF552	20/20/200/200	JF669	4th	0.2
11	458568	5/21/19	8/8/19	GFP	10/24/19	JF570	20/20/200/200	JF669	4th	0.05
13	460147	7/13/19		MeCP2-F	1/15/20	JF669	40/0/60/100	JF585	24th	
13	460149	7/13/19		MeCP2-F	1/15/20	JF669	20/20/60/100	JF585	24th	
13	467293	6/1/19		MeCP2-M	1/15/20	JF669	40/0/60/100	JF585	24th	
13	467294	6/1/19		MeCP2-M	1/15/20	JF669	20/20/60/100	JF585	24th	
13	467295	6/1/19		MeCP2-M	1/15/20	JF669	40/0/60/100	JF585	24th	
13	467296	6/1/19		MeCP2-M	1/15/20	JF669	20/20/60/100	JF585	24th	
14	456996	6/1/19		MeCP2-F	2/10/20	JF669	20/20/60/100	JF585	24th	
14	456997	6/1/19		MeCP2-F	2/10/20	JF669	0/40/60/100	JF585	24th	
14	456998	6/1/19		MeCP2-F	2/10/20	JF669	10/30/60/100	JF585	24th	

14	456999	6/1/19		MeCP2-F	2/10/20	JF669	0/60/40/100	JF585	24th	
14	457000	6/1/19		MeCP2-F	2/10/20	JF669	0/80/20/100	JF585	24th	

950

951 # Supplementary Movies

952 **Supplementary Movie 1 –** Injection of dye at a slow rate (20 µl/min). See Supplementary
953 Fig. 4 and methods for details.

954 **Supplementary Movie 2 –** Injection of dye at a faster rate (40 µl/min). See Supplementary
955 Fig. 4 and methods for details.

956 **Supplementary Movie 3 –** Imaging single synapses in layer 1 of cortex using ExM and
957 Airyscan imaging. See Figure 2i and Methods for details.

958 **Supplementary Movie 4 –** Imaging single synapses in CA3 subfield of the hippocampus
959 using ExM and Airyscan imaging. See Figure 2i and methods for details.